



Synthesis of rGO-doped $\text{Nb}_4\text{O}_5\text{--TiO}_2$ nanorods for photocatalytic and electrochemical energy storage applications

Rajesh Rajagopal, Kwang-Sun Ryu*

Department of Chemistry and Energy Harvest Storage Research Center (EHSRC), University of Ulsan, Ulsan 680-749, South Korea



ARTICLE INFO

Keywords:
 $\text{Nb}_4\text{O}_5\text{--TiO}_2$
 Reduced graphene oxide
 Photocatalyst
 Supercapacitor

ABSTRACT

A novel $(\text{Nb}_4\text{O}_5\text{--TiO}_2)\text{@rGO}$ nanocomposite was synthesized using a Na^+ ion intercalation-assisted hydrothermal technique and examined its photocatalyst dye degradation and supercapacitor applications. The synthesized $(\text{Nb}_4\text{O}_5\text{--TiO}_2)$ nanorods were segregated by well dispersed reduced graphene oxide with different weight ratios. A strong interaction was observed between the $(\text{Nb}_4\text{O}_5\text{--TiO}_2)$ to rGO nanosheets, even with high rGO content (5 wt. %). Experiments examining the photocatalytic degradation of methylene blue suggested that the $(\text{Nb}_4\text{O}_5\text{--TiO}_2)\text{@ 5rGO}$ nanocomposites exhibit excellent charge carrier mobility with a higher methylene blue degradation rate (92%) than $\text{Nb}_4\text{O}_5\text{--TiO}_2$ nanorods and other $(\text{Nb}_4\text{O}_5\text{--TiO}_2)\text{@rGO}$ nanocomposites under ultraviolet and visible light irradiation. On the other hand, the $(\text{Nb}_4\text{O}_5\text{--TiO}_2)\text{@ 5rGO}$ nanocomposite exhibited excellent electrochemical performance with high specific capacitance (365 F g^{-1}), long cycling stability ($\sim 100\%$ capacitance retention after 1000 cycles), and good rate capability (70% capacitance retention at 25 A g^{-1}). In addition, the photocatalytic and supercapacitor efficiency of the $(\text{Nb}_4\text{O}_5\text{--TiO}_2)\text{@rGO}$ nanocomposite increased gradually with increasing amount of rGO in the composite. These features collectively demonstrated the high rate of photocatalytic degradation efficiency and good energy storage performance of the $(\text{Nb}_4\text{O}_5\text{--TiO}_2)\text{@ 5rGO}$ nanocomposite, which suggests a new route for large scale applications in energy and environmental fields.

1. Introduction

The continued industrialization is dependent on fossil fuels for all energy needs. Unfortunately, these fossil fuels emit many pollutants that contaminate the air and water bodies [1]. Many conventional methods have been developed to remove pollutants but they only transferred the pollutant from one phase (liquid) to another (solid), and an additional process is needed to remove the waste. Therefore, it is essential to develop new technologies/devices for complete green energy production and purification [2]. Considerable efforts have been made to develop purification, green energy generation, and storage technologies/devices [3,4]. Over the past decade, advanced oxidation processes (AOP) have been proposed to remove the organic pollutants from wastewater and air [5–7]. Recent studies have reported that semiconductor nanostructures show better performance than bulk semiconducting materials and are suitable for environment and energy storage applications through the AOP process and ion adsorption process, respectively [8–10]. Semiconductor nanostructure-based photocatalysts can separate the harmful materials from wastewater using solar irradiation. These semiconducting photocatalytic materials should

be non-toxic, low cost, environmentally friendly, stable in water solution, and easy to synthesize [11]. Concentrating on energy storage devices, supercapacitors have attracted increasing attraction owing to its superior power density than batteries and high energy density than other conventional electrostatic and electrolytic capacitors. In addition, these supercapacitors are safer than batteries and have low environmental impact [1].

A large variety of metal oxide and metal sulfide semiconducting nanostructures have been used for photocatalytic and supercapacitor applications. Among the diverse range of semiconducting nanostructures, titanium dioxide (TiO_2) and its nano-heterostructures have many advantages because of its low toxicity, high stability, large availability, and useful physico – chemical properties. Thus, TiO_2 and its heterostructures are used widely in many applications, such as photocatalysts, supercapacitors, solar cells, fuel cells, sensors, batteries, and water treatment [12–14]. In particular, the wide band gap, photo absorption property, charge carrier mobility, and structural flexibility make it a suitable material to solve existing energy and environmental issues. One dimensional TiO_2 nanostructures (tubes, wires, rods, etc.) have attracted enormous interest owing to their high surface area to

* Corresponding author.

E-mail address: ryuks@ulsan.ac.kr (K.-S. Ryu).

volume ratio, fast and long distance electron transport property, and high photoconductivity [4,15]. On the other hand, high resistivity and wide band gap (~ 3.2 eV) limit the use of pure TiO_2 nanostructures in energy storage and photocatalytic applications. This is because the high resistivity increases the internal resistance of the electrodes in charge storage devices and increases the likelihood of electron – hole recombination when used as a photocatalyst [16,17]. To overcome these limitations, researchers have focused on the development of modified/doped TiO_2 nanostructures. In connection to this, pure TiO_2 nanostucture have been doped with various metallic elements, nonmetallic elements, and other narrow band gap semiconducting materials to increase the efficiency towards photocatalytic and energy storage applications. Interestingly, niobium-doped TiO_2 has received considerable attention among the scientific community because of its wide range of applications [18]. Many research groups synthesized Nb-doped TiO_2 for energy and environmental applications. Yan et al. developed an $\text{Nb}_2\text{O}_5/\text{TiO}_2$ heterojunctions using an *in situ* hydrolysis loading process and examined the photocatalytic activity according to the Nb loading on Ti [19]. Similarly, Bhachu et al. synthesized Nb:TiO₂ thin films through a solution processing route and analyzed its photocatalysts, electrical conductivity, optical transparency, and blue coloration properties [20]. Vidyadharan et al. studied the supercapacitance property of niobium doped titania nanowires produced from an electro spinning process [21]. Bauer et al. also prepared Mn and Mo-doped TiO_2 and examined their Li ion storage behavior [22]. The addition of niobium generates a new donor energy level just below the conduction band of TiO_2 ; thus, the electronic transition occurred from the valance band to these donor levels by consuming less energy. Nevertheless, some deep level electrons are not involved in these transitions; thus, enhanced charge separation is needed for Nb-doped TiO_2 materials.

To enhance the efficiency of TiO_2 semiconducting nanostructures towards the photocatalytic and supercapacitor applications, many research groups have focused on the incorporation of carbonaceous materials [23,24]. In particular, graphene materials have attracted more interest than other nanocarbon materials owing to its high surface area, high charge carrier mobility, and high mechanical stability [25]. When graphene materials are mixed with TiO_2 semiconducting nanostructures, it acts as a best supporting material, non-aggregation of nanoparticles, enhanced electron transfer, and used to separate the photo generated electron – hole pairs. Many graphene – semiconductor nanostructure composites have been reported to improve the efficiency of the photocatalyst and supercapacitor electrodes [26–28]. Pure TiO_2 or doped TiO_2 – graphene nanocomposites are recognized as an efficient photocatalyst and there has been considerable interest on supercapacitor applications. Min et al. synthesized strongly coupled TiO_2 /graphene quantum dots using simple hydrothermal techniques and applied them as a photocatalyst towards hydrogen production [29]. Similarly, Jo et al. synthesized cobalt-doped TiO_2/rGO and studied its oxytetracycline and Congo red degradation efficiency in solar and visible light irradiation [30]. The ion-intercalated hydrothermal synthesis of $\text{Nb}_2\text{O}_5\text{-TiO}_2$ was synthesized and a $\text{Nb}_2\text{O}_5\text{-TiO}_2/\text{rGO}$ sandwich type electrode was developed for supercapacitor applications [31]. Thus, various combination of rGO doped TiO_2 and niobium doped TiO_2 nanocomposites were prepared and studied for photocatalytic application. To the best of the authors' knowledge, niobium and rGO co-doped TiO_2 nanocomposite have not been reported for photocatalytic application. Specifically, the synthesis of $\text{Nb}_4\text{O}_5\text{-TiO}_2$ and various weight ratio of rGO doped $\text{Nb}_4\text{O}_5\text{-TiO}_2$ and the strategy of using these materials as active photocatalysts and supercapacitor electrodes have not been reported. In addition, this tetragonal latticed tetranioibium pentoxide (Nb_4O_5) is differing from other niobium oxide composites due to its novel equilibrium phase. The Nb_4O_5 material show more Nb – Nb metallic bonds which may increased the TiO_2 lattice disorder and creates new states in the electronic structure of TiO_2 nanomaterials. As a result, the rate of electron trapping will be improved and inhibit the electron – hole recombination during the

irradiation process. This decrease in electron – hole recombination leads the enhanced photocatalytic activity [32–34].

This paper reports the synthesis of pure TiO_2 , $\text{Nb}_4\text{O}_5\text{-TiO}_2$, and $\text{Nb}_4\text{O}_5\text{-TiO}_2@/\text{rGO}$ using an ion intercalation-assisted hydrothermal method and explored its environment and energy applications as efficient photocatalyst and supercapacitor electrode materials. The synthesized materials were used as a photocatalyst to degrade methylene blue under ultraviolet and visible light irradiation. The effects of rGO mixing with the novel photocatalyst was examined and $(\text{Nb}_4\text{O}_5\text{-TiO}_2)@5\text{rGO}$ showed high methylene blue degradation photocatalytic activity. The MB degradation efficiency of $(\text{Nb}_4\text{O}_5\text{-TiO}_2)@5\text{rGO}$ was 92%, which is 1.53 and 1.24 times higher than the pure TiO_2 and $\text{Nb}_4\text{O}_5\text{-TiO}_2$ photocatalysts, respectively. In addition, compared to pure TiO_2 and $\text{Nb}_4\text{O}_5\text{-TiO}_2$ electrode materials, $(\text{Nb}_4\text{O}_5\text{-TiO}_2)@5\text{rGO}$ exhibited a high specific capacitance of 365 F g^{-1} at 5 A g^{-1} in a 1 M Na_2SO_4 aqueous electrolyte. These unique properties of $(\text{Nb}_4\text{O}_5\text{-TiO}_2)@5\text{rGO}$ showed higher photocatalytic activity towards MB degradation under UV and visible light irradiation as well as a higher specific capacitance.

2. Experimental

TiO_2 powder (anatase, $\geq 99\%$), sodium hydroxide (NaOH, 98%), hydrochloric acid (HCl, 37%), niobium ethoxide ($\text{Nb}_2(\text{OC}_2\text{H}_5)_5$, 99.95%), graphite powder ($> 45\text{ }\mu\text{m}$, 99.99%), sulphuric acid (H_2SO_4 , 95–98%), potassium permanganate (KMnO_4 , 97%), hydrogen peroxide (H_2O_2 , 30%), hydrogen hydrate ($\text{N}_2\text{H}_4\text{H}_2\text{O}$, 60%) and sodium sulfate (Na_2SO_4 , $\geq 99\%$) were all obtained from Sigma Aldrich. methylene blue ($\text{C}_{16}\text{H}_{18}\text{ClN}_3\text{S}\text{-}3\text{H}_2\text{O}$, 97%), Ethanol and acetone were purchased from Daejung chemicals. All the chemicals were used as received without any purification.

2.1. Synthesis of $\text{Nb}_4\text{O}_5\text{-TiO}_2$ nanocomposite

TiO_2 nanorods were synthesized using the following procedure [35]. First, 4 g of TiO_2 was dispersed in 70 ml of 10 M NaOH solutions and sonicated for 30 min. The above mixture was treated hydrothermally at 160 °C for 48 h. After the filtration and drying process, the above product (1 g) was dispersed in a 1 M HCl solution and sonicated for 15 min. The mixture was transferred to a Teflon-lined autoclave and treated hydrothermally at 100 °C for 1 h. The product was then cooled to room temperature, washed with large amounts of water, and dried in air. The above hydrothermal treatment was repeated three times to remove sodium ions and replace the hydrogen atoms. The Nb_4O_5 -mixed TiO_2 nanorods were synthesized using the following procedure. Hydrogenated TiO_2 (0.2 g) was dispersed in 10 ml of ethanol and stirred for 1 h. Subsequently, 0.5 g of niobium ethoxide and 0.1 ml of conc. HCl was added with vigorous stirring. H_2O (1 ml) was added to the above mixture and stirred until gel formation. Finally, the above gel mixture was heat-treated at 600 °C for 1 h at an increasing heat rate of 100 °C/h. Finally, the product of $\text{Nb}_4\text{O}_5\text{-TiO}_2$ was collected from the furnace and used for further process.

2.2. Synthesis of reduced graphene oxide material

A reduced graphene oxide material was synthesized from graphite powder using a modified Hummer's method [31]. Commercially purchased graphite powder (1 g) was immersed in 50 ml of concentrated H_2SO_4 and stirred for 30 min. The mixture was then cooled to $< 5\text{ }^\circ\text{C}$ in an ice bath and stirred for 1 h. Subsequently, 6 g of KMnO_4 was added carefully to the above mixture with constant stirring. During the process the reaction temperature was maintained at $< 15\text{ }^\circ\text{C}$. After continuous stirring for 2 h, 90 ml of distilled water was added to the mixture. During the addition of water, the reaction temperature was maintained below 35 °C and stirred for a further 2 h. Finally, 280 ml of H_2O_2 was added quickly and 6 ml of H_2O_2 was then added drop wise

with vigorous stirring. The synthesized graphene oxide (GO) was washed with water and a 10% HCl solution, and the filtered GO was then dried in an oven. The reduced graphene oxide was obtained using a chemical reduction method similar to previous work. Briefly, 50 mg of synthesized graphene oxide were dispersed in 50 ml of double distilled water. Then 1 ml of hydrogen hydrated solution was added and continuously stirred at 70 °C for 8 h. Finally, the mixture was washed with 3 liters of water followed by ethanol and filtered. The reduced graphene oxide was air dried at 80 °C for 12 h and used for electrode fabrication.

2.3. Synthesis of $\text{Nb}_4\text{O}_5\text{-TiO}_2\text{@rGO}$ composite

The $\text{Nb}_4\text{O}_5\text{-TiO}_2\text{@rGO}$ composite was obtained by a facile hydrothermal process. First, 2 mg of reduced graphene oxide (1 wt. %) was dispersed in 100 ml of ethanol/water (20 ml/80 ml) solution and sonicated for 10 min. Subsequently, 200 mg of the $\text{Nb}_4\text{O}_5\text{-TiO}_2$ nanocomposite was dispersed in the above solution and sonicated for 30 min. The mixture treated hydrothermally at 100 °C for 12 h to obtain the $\text{Nb}_4\text{O}_5\text{-TiO}_2\text{@rGO}$ composite. Finally, the product was filtered and dried in air. The resulting product was called $\text{Nb}_4\text{O}_5\text{-TiO}_2\text{@ 1rGO}$ and the same procedure was adapted to synthesis, $\text{Nb}_4\text{O}_5\text{-TiO}_2\text{@ 2rGO}$, $\text{Nb}_4\text{O}_5\text{-TiO}_2\text{@ 3rGO}$, $\text{Nb}_4\text{O}_5\text{-TiO}_2\text{@ 4rGO}$ and $\text{Nb}_4\text{O}_5\text{-TiO}_2\text{@ 5rGO}$ by changing the rGO concentration of 2, 3, 4, and 5 wt. %.

2.4. Characterization of $\text{Nb}_4\text{O}_5\text{-TiO}_2\text{@rGO}$ composite

The physicochemical properties of the TiO_2 , $\text{Nb}_4\text{O}_5\text{-TiO}_2$, $\text{Nb}_4\text{O}_5\text{-TiO}_2\text{@rGO}$ nanocomposites were examined. Powder X-ray diffraction (XRD, Rigaku-Ultima (IV)) of the synthesized nanomaterials was performed using $\text{Cu K}\alpha$ radiation. Nitrogen adsorption – desorption isotherm were measured at -196.15 °C using a nanoPOROSTY surface area analyzer (Miarscientific instruments, Inc.). Prior to analysis, the synthesized materials were degassed at 200 °C for 3 h. The specific surface area was calculated using the Brunauer–Emmett–Teller (BET) method and Barrett–Joyner–Halenda (BJH) theory was used to calculate the pore size distribution. The functional groups of the synthesized nanocomposite materials were analyzed by Fourier transform infrared (FTIR, IR Affinity-IS, Shimadzu) spectroscopy. Morphology and elemental composition analysis were performed by field emission scanning electron microscopy (FESEM, Jeol-JSM7600F) equipped with an energy dispersive X-ray spectroscopy (EDX). High resolution transmission electron microscopy (TEM, Jeol- JEM-2100F) was performed at an accelerating voltage of 200 kV. The surface components and their valance distributions were analyzed by Thermo scientific X-ray photoelectron spectroscopy (XPS) using an $\text{Al K}\alpha$ monochromatized X-ray source. The UV-vis diffused reflectance spectra of the synthesized nanocomposites were recorded on Shimadzu UV – 2450 UV-vis diffuse reflectance spectrophotometer.

2.5. Photocatalytic experiments

The standard model pollutant methylene blue was used to examine the photodegradation efficiency of the synthesized materials. A 6 W ultra violet lamp (Philips) and 6 W visible light lamp (Philips) were used as the irradiation sources. All the degradation experiments were carried out under atmospheric conditions with a constant stirring speed of 250 rpm. In a typical experiment, 50 mg of catalyst was dispersed in 150 ml of an aqueous MB solution (10 mg/L) and sonicated for 10 min. Before the light irradiation, the catalyst containing MB solution was stirred for 30 min in the dark. The catalyst and MB solution mixture was then stirred under UV/visible light irradiation. During the degradation process, 5 ml of the solution was removed from the mixture and centrifuged for 15 min in 3500 rpm. Finally, the supernatant was collected and the concentration of MB was analyzed by UV-vis. spectrophotometer. The degradation efficiency of the catalyst was calculated using the following equation [36]:

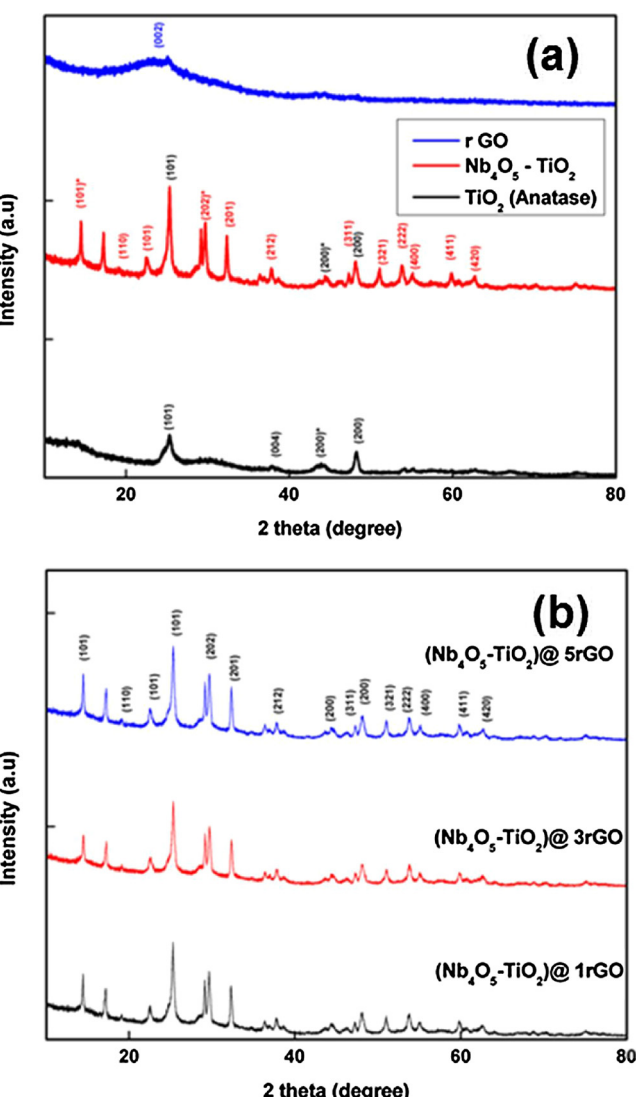


Fig. 1. Powder XRD pattern of (a) TiO_2 , $\text{Nb}_4\text{O}_5\text{-TiO}_2$, rGO and (b) $(\text{Nb}_4\text{O}_5\text{-TiO}_2)\text{@rGO}$ nanocomposites.

$$\text{Degradation Efficiency (\%)} = \frac{C_0 - C}{C_0} \times 100$$

where C_0 and C is the concentration of initial and degraded MB solution, respectively.

2.6. Electrochemical measurements of the $\text{Nb}_4\text{O}_5\text{-TiO}_2\text{@rGO}$ composite

For the electrochemical measurements, the active working electrode was prepared by an electrophoretic deposition process. Briefly, 1 mg of the synthesized material was dispersed in 20 ml of a 1 mmol $\text{Mn}(\text{NO}_3)_2\text{·}4\text{H}_2\text{O}$ ethanol solution and sonicated for 10 min. After sonication, two platinum strips (20 mm x 3 mm x 0.5 mm) were immersed in the solution (10 mm depth) and a D.C voltage of 24 V was applied between the platinum strips for 5 min. The electrochemical behavior of the layered electrodes was examined by cyclic voltammetry (CV), charge – discharge and electrochemical impedance spectroscopy (EIS) using an IVIUMSTAT instrument. A pure platinum strip and Ag/AgCl in saturated KCl were used as the counter and reference electrodes, respectively. The cyclic voltammograms of the electrodes were recorded from 20 mV to 100 mV (20 mV interval). Similarly, the charge-discharge behavior of the electrodes was recorded at current densities of 5 A/g, 10 A/g, 50 A/g, 20 A/g, 25 A/g, and 50 A/g. All electrochemical

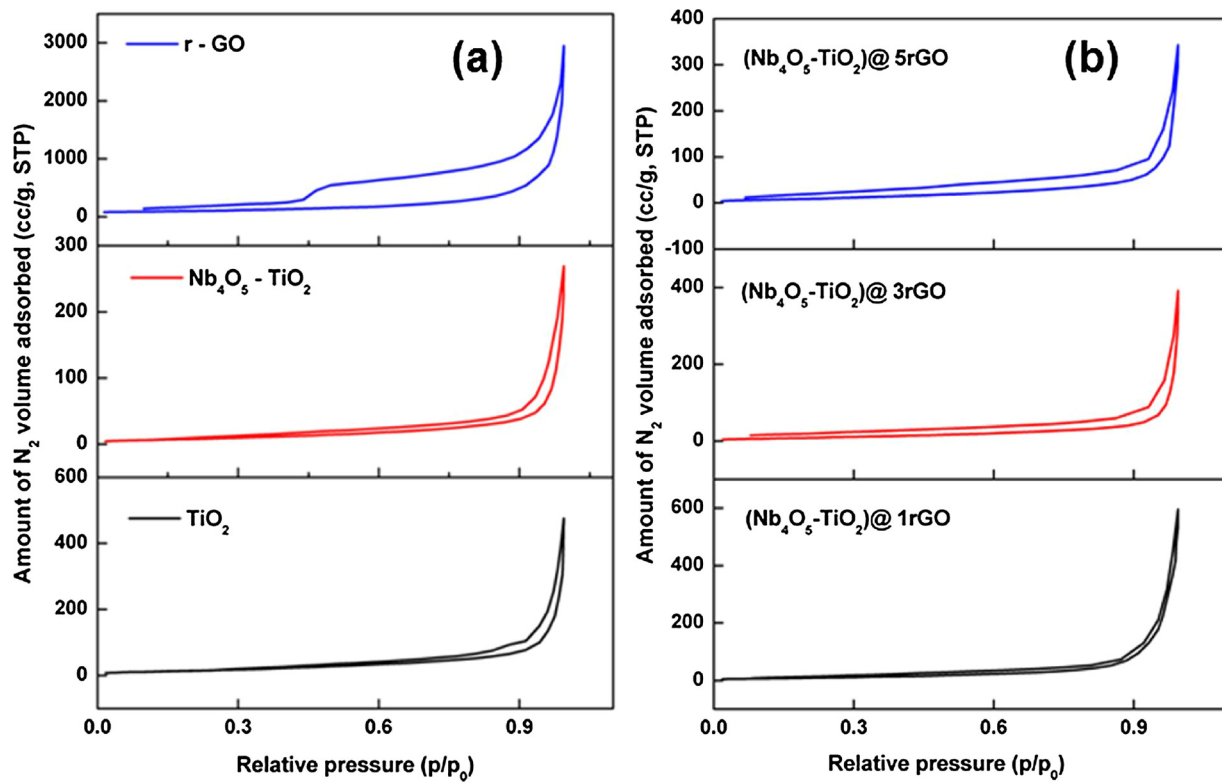


Fig. 2. Nitrogen adsorption – desorption isotherm of (a) TiO₂, Nb₄O₅–TiO₂, rGO and (b) (Nb₄O₅–TiO₂)@rGO nanocomposites.

Table 1

Nitrogen adsorption studies of TiO₂, Nb₄O₅–TiO₂ and Nb₄O₅–TiO₂@rGO nanocomposites.

Sample	Surface area (m ² g ⁻¹)	Pore size (nm)	Pore volume cc g ⁻¹
TiO ₂	57.51	8.26	0.64
Nb ₄ O ₅ –TiO ₂	30.46	7.46	0.36
rGO	342.16	5.10	4.40
(Nb ₄ O ₅ –TiO ₂)@ 1rGO	36.26	8.22	0.70
(Nb ₄ O ₅ –TiO ₂)@ 3rGO	36.34	5.33	0.42
(Nb ₄ O ₅ –TiO ₂)@ 5rGO	37.58	4.45	0.30

measurements were conducted in 0.5 M aqueous Na₂SO₄ solutions under ambient temperature and pressure conditions.

3. Results and discussion

3.1. Phase structural and morphological analysis

The phase structural properties of the synthesized Nb₄O₅–TiO₂ and Nb₄O₅–TiO₂@rGO nanocomposites were examined by powder XRD, and N₂ adsorption– desorption techniques. Fig. 1a presents the XRD pattern of the prepared TiO₂, Nb₄O₅–TiO₂, and rGO materials. A typical XRD pattern of anatase TiO₂ was observed in the synthesized pure TiO₂ nanorods, which was well matched with the JCPDS card number of 01-070-6826 [37]. The peaks at 25.5°, 37.8°, and 48.2° 2θ were indexed to the (101), (004), and (200) crystal planes, respectively. The crystalline structure of TiO₂ was still unchanged, even after the addition of niobium species; this is due to the surface anchored niobium oxide nanoparticles. From the XRD pattern of the Nb₄O₅–TiO₂ nanocomposites, the characteristic peaks of tetragonal tetranioibium pentoxide (Nb₄O₅) were observed at 19.1°, 22.5°, 32.3°, 37.8°, 47.2°, 51.1°, 53.9°, 55.0°, 59.9°, and 62.6° 2θ corresponding to the (110), (101), (201), (212), (311), (321), (222), (400), (411) and (420) crystal plane, respectively. The

peaks for Nb₄O₅ well matched the JCPDS card number of 01-077-0844 with the space group of P42/nmc. In addition, peaks at 14.3° and 29.7° were observed due to the presence of dititanium hexaniobiate (Ti₂(Nb₆O₁₂)) and the corresponding crystalline planes were (101) and (202), respectively. Similarly, a peak at 44.4° (200) was observed in both TiO₂ and the TiO₂–Nb₄O₅ nanocomposite, which correspond to the existence of a Hongquite TiO crystalline phase. The characteristic peak of graphite was observed at 24.7° (002) from the XRD pattern of reduced graphene oxide [38]. Fig. 1b shows the XRD pattern of Nb₄O₅–TiO₂@ 1rGO, Nb₄O₅–TiO₂@ 3rGO and Nb₄O₅–TiO₂@ 5rGO. The XRD pattern of Nb₄O₅–TiO₂@rGO was similar to the pattern of the Nb₄O₅–TiO₂ nanocomposite and no changes in the peaks were observed. The graphitic peak disappeared in all Nb₄O₅–TiO₂@rGO composites, suggesting that the Nb₄O₅–TiO₂@rGO nanocomposite was loaded on the surface of the rGO nanosheets.

The specific surface area and porosity of the synthesized nanocomposites were evaluated from nitrogen adsorption – desorption analysis and the corresponding isotherm was presented in Fig. 2(a & b). The isotherm graphs show that all the materials exhibited a type IV isotherm with an obvious hysteresis loop, confirming the existence of mesopores [39]. The specific surface area of pure TiO₂ is 57.51 m² g⁻¹, which was reduced to 30.46 m² g⁻¹ (Nb₄O₅–TiO₂), while adding the Nb₄O₅ nanoparticles. This is because the Nb₄O₅ nanoparticles decorated over the surface of the TiO₂ nanorods and increased the volume of the one dimensional nanorods. The synthesized reduced graphene oxide material exhibited a relatively high surface area of 342.16 m² g⁻¹, which was ten times larger than that of the pure TiO₂ and Nb₄O₅–TiO₂ nanocomposites. The specific surface area of rGO mixed (Nb₄O₅–TiO₂) increased gradually with increasing amount of rGO. All the nanocomposites showed a narrow isotherm at the mid-relative pressure region (p/p₀ = 0.3 to 0.7), indicating the presence of a uniform pore size distribution [40]. The mean pore size and pore volume of all materials were calculated using the BJH desorption technique; the values are listed in Table 1. The pore size and pore volume of pure TiO₂ is 8.26 nm and 0.64 cc g⁻¹, which was reduced to 7.46 nm and

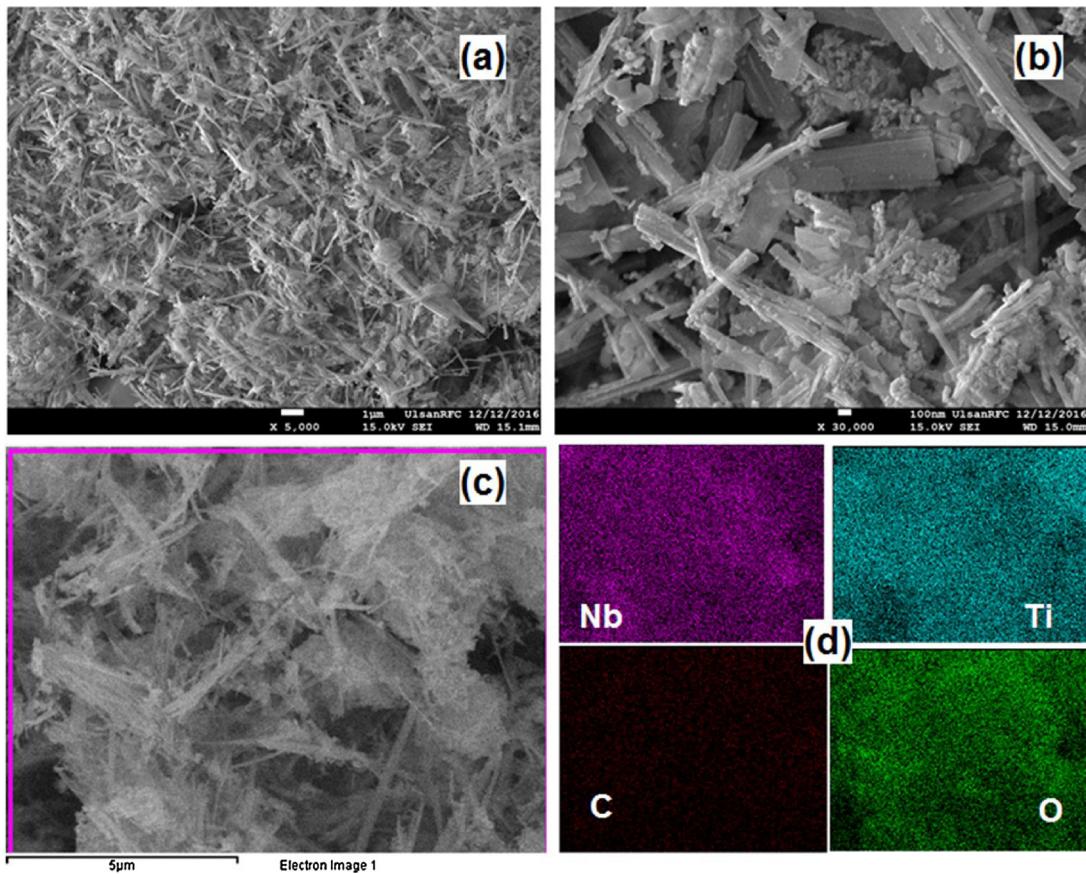


Fig. 3. (a&b) FESEM images of $(\text{Nb}_4\text{O}_5\text{--TiO}_2)@3\text{rGO}$ at different magnifications and (c&d) EDS mapping of the $(\text{Nb}_4\text{O}_5\text{--TiO}_2)@r\text{GO}$ nanocomposite with Nb, Ti, C and O elements.

0.36 cc g⁻¹ while decorating with Nb_4O_5 nanoparticles. Similarly, addition of reduced graphene oxide decrease the pore size of $\text{Nb}_4\text{O}_5\text{--TiO}_2$ nanocomposite from 8.22 nm ($(\text{Nb}_4\text{O}_5\text{--TiO}_2)@1\text{rGO}$) to 4.45 nm ($(\text{Nb}_4\text{O}_5\text{--TiO}_2)@5\text{rGO}$). When adding/mixing the dopant (Nb_4O_5 and rGO) with the pure TiO_2 , the pore size decreased significantly due to the blocking of foreign materials.

The surface morphology and microstructure of the as-prepared $(\text{Nb}_4\text{O}_5\text{--TiO}_2)@3\text{rGO}$ nanocomposite was examined by FESEM and TEM. Fig. 3a & b shows FESEM images of $(\text{Nb}_4\text{O}_5\text{--TiO}_2)@3\text{rGO}$ at two different magnifications. FESEM revealed the formation of irregular sized TiO_2 nanorods, ranging in length from $\sim 1\text{ }\mu\text{m}$ to $10\text{ }\mu\text{m}$ with surface-anchored aggregated Nb_4O_5 nanoparticles. The surface of the nanorods was not smooth, indicating the porous nature of the material. The reduced graphene oxide nanosheets were fully mixed with the $\text{Nb}_4\text{O}_5\text{--TiO}_2$ nanocomposite, and no stacked layers of rGO nanosheets were observed. This proves that the hydrothermal process helped separate the rGO nanosheets and the intercalation of the $\text{Nb}_4\text{O}_5\text{--TiO}_2$ nanocomposite. Moreover, EDX elemental mapping of the $(\text{Nb}_4\text{O}_5\text{--TiO}_2)@3\text{rGO}$ nanocomposite confirmed the good distribution of Nb, Ti, C, and O, which are illustrated in Fig. 3(c & d).

The as-synthesized $(\text{Nb}_4\text{O}_5\text{--TiO}_2)@3\text{rGO}$ nanocomposite was investigated further by TEM; the corresponding images are shown in Fig. 4(a-d). As shown in Fig. 4a-c, Nb_4O_5 was anchored on the TiO_2 surface and the $\text{Nb}_4\text{O}_5\text{--TiO}_2$ nanocomposite was wrapped with rGO nanosheets. The TiO_2 nanorods were composed of many layers but no isolated Nb_4O_5 nanoparticles and rGO nanosheets were observed. This is because the interactions between TiO_2 to Nb_4O_5 and $\text{Nb}_4\text{O}_5\text{--TiO}_2$ to rGO nanosheets were very high, and they were unaffected by the strong ultrasonication during TEM sample preparation. This strong interaction can be explained by the relatively small size and surface distribution of Nb_4O_5 nanoparticles. Higher magnifications showed that the

aggregated Nb_4O_5 nanoparticles are in strong contact with the TiO_2 crystal lattice (Fig. 4d). These strong mutual interactions between the Nb_4O_5 , TiO_2 , and rGO nanosheets increase the electron transport property rapidly. Therefore, the introduction of rGO nanosheets effectively separates the Nb_4O_5 -anchored TiO_2 nanorods and vice versa, which could improve the efficiency for energy and environmental applications.

Fig. 5a & b shows the FTIR spectra of TiO_2 , $\text{Nb}_4\text{O}_5\text{--TiO}_2$, and rGO and $(\text{Nb}_4\text{O}_5\text{--TiO}_2)@r\text{GO}$ nanocomposites. The FTIR spectra of TiO_2 showed a broad peak at approximately 500 cm^{-1} , which was assigned to the Ti--O--Ti stretching vibrations and a wide peak approximately 3500 cm^{-1} due to the O--H stretching vibrations (Fig. 5a) [41]. In $\text{Nb}_4\text{O}_5\text{--TiO}_2$, a small peak was observed near 1000 cm^{-1} , which may originate from the Nb--O vibration [42]. In the case of reduced graphene oxide, the characteristic peaks at 1239 cm^{-1} and 1716 cm^{-1} were attributed to the C--O--H and C=O stretching vibrations, respectively [31]. Fig. 5b shows the FTIR spectra of $(\text{Nb}_4\text{O}_5\text{--TiO}_2)@1\text{rGO}$, $(\text{Nb}_4\text{O}_5\text{--TiO}_2)@3\text{rGO}$, and $(\text{Nb}_4\text{O}_5\text{--TiO}_2)@5\text{rGO}$ nanocomposites. The intensities of the peaks for Nb--O and Ti--O--Ti decreased dramatically with increasing rGO concentration and were absent in the $(\text{Nb}_4\text{O}_5\text{--TiO}_2)@5\text{rGO}$ nanocomposites. Therefore, during the hydrothermal process, the carboxylic groups of rGO interacted with the surface hydroxyl groups of $\text{Nb}_4\text{O}_5\text{--TiO}_2$.

XPS was performed to analyze the surface chemical composition and electronic states of Nb and Ti in the $(\text{Nb}_4\text{O}_5\text{--TiO}_2)@3\text{rGO}$ nanocomposite, as shown in Fig. 5(c-f). Strong photoelectron peaks of Nb (3d), Ti (2p), C (1s), and O (1s) were observed from the XPS survey spectrum (Fig. 5c) of the $(\text{Nb}_4\text{O}_5\text{--TiO}_2)@3\text{rGO}$ nanocomposite. This confirmed that the ternary composite of $(\text{Nb}_4\text{O}_5\text{--TiO}_2)@r\text{GO}$ had been synthesized successfully. Fig. 5d shows that the Nb (3d) has two peaks at 207.65 eV ($3\text{d}_{5/2}$) and 210.40 eV ($3\text{d}_{5/2}$) with 2.75 eV spin orbit

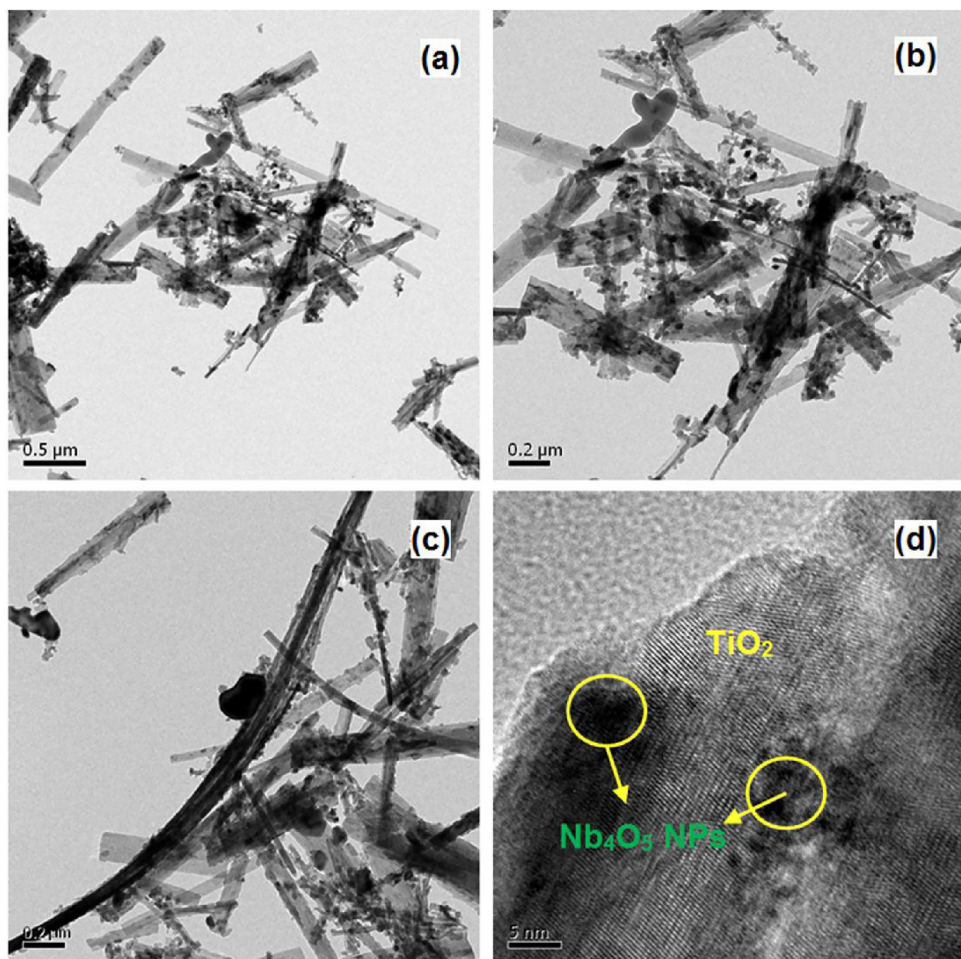


Fig. 4. (a-d) HRTEM images of $(\text{Nb}_4\text{O}_5\text{-TiO}_2)@3\text{rGO}$ at different magnifications.

splitting, which were assigned to the Nb^{5+} core levels [43]. Similarly, the Ti^{4+} core levels were confirmed by the presence of characteristic peaks at 459.36 eV ($2\text{p}_{3/2}$) and 465.10 eV ($2\text{p}_{1/2}$) with spin orbital splitting of 5.74 eV, as shown in Fig. 5e [44]. No other peaks were observed in high resolution Ti (2p) and Nb (3d) spectrum. Fig. 5f shows the high resolution C (1s) spectrum, which has two component peaks located at 285.5 eV and 289.4 eV, which were assigned to aromatic rings ($\text{C}=\text{C}$) and carboxyl group ($\text{O}-\text{C}-\text{O}$), respectively [45]. This weakened carboxyl group confirmed the reduction of rGO and enables the strong interaction between rGO and the $\text{Nb}_4\text{O}_5\text{-TiO}_2$ nanorods. The peak intensity of $\text{C}=\text{C}$ was much higher than that of the $\text{O}=\text{C}-\text{O}$ peak, suggesting a high degree of the reduction process. The inset in Fig. 5f shows the high resolution spectrum of O (1s) with a sharp peak at 530.74 eV, which was assigned to surface oxygen.

3.2. Diffuse reflectance spectroscopy analysis

Diffuse reflectance spectroscopy was used to examine the optical band gap of TiO_2 , $\text{Nb}_4\text{O}_5\text{-TiO}_2$ and $(\text{Nb}_4\text{O}_5\text{-TiO}_2)@3\text{rGO}$ materials (Fig. 6a). Kubelka-Munk's function was used to calculate the band gap of these materials, as shown in Fig. 6b. The TiO_2 and its rGO composites showed the typical DRS spectra of semiconductors. The calculated band gap of pure TiO_2 is 3.277 eV; after adding niobium oxide, the band gap decreased slightly to 3.269 eV. The addition of Nb_4O_5 and rGO produced a red shift with increasing concentration and the band gap of 1, 2, 3, 4 and 5 wt. % rGO added $\text{Nb}_4\text{O}_5\text{-TiO}_2$ was 3.256, 3.256, 3.242, 3.235, and 3.221 eV respectively. Therefore, the band gap of all composites was slightly lower than that of pure TiO_2 , indicating the underlying reduced graphene oxide on the pure TiO_2 domains [46]. For

pure rGO, a horizontal line (not shown) was observed, indicating poor reflectance performance. In addition, the decrease in band gap is due to hybridization between the 2p orbitals of C and O atoms; an impurity energy level is generated just above the valence band [47]. Therefore, the photo response range was increased significantly and the photocatalytic behavior was improved greatly.

3.3. Photocatalytic activity

The photocatalytic activity of the synthesized pure TiO_2 , $\text{Nb}_4\text{O}_5\text{-TiO}_2$, and $(\text{Nb}_4\text{O}_5\text{-TiO}_2)@3\text{rGO}$ composite were evaluated by the degradation of a model pollutant, MB, in aqueous solution with ultraviolet and visible light irradiation at room temperature. Fig. 7a shows the UV absorption spectrum of the methylene blue solution at various UV light irradiation times with the $(\text{Nb}_4\text{O}_5\text{-TiO}_2)@5\text{rGO}$ photocatalyst. As shown in Fig. 7a, the characteristic absorption peak of MB was observed at 291.8, 614.6, and 662.5 nm. The absorbance peak height of MB was quenched gradually with respect to the UV irradiation time and the color changes indicate the photocatalytic decomposition of the MB chromophoric structure [46]. The adsorption capability and photo-degradation efficiency (C/C_0) of all photocatalyst materials were evaluated under UV irradiation and is presented in Fig. 7b. The adsorption experiment in the dark showed that the addition of rGO nanosheets gradually elevates the adsorption capacity and reached 47% at the end of 5 wt. % rGO addition. The relatively large surface of reduced graphene oxide enables this high adsorption character. Initially, pure TiO_2 nanorods showed poor degradation efficiency of 60% (180 min.), which was improved to 74% (180 min.) by adding Nb_4O_5 nanoparticles. As discussed earlier, the addition of rGO nanosheets reduced the band gap

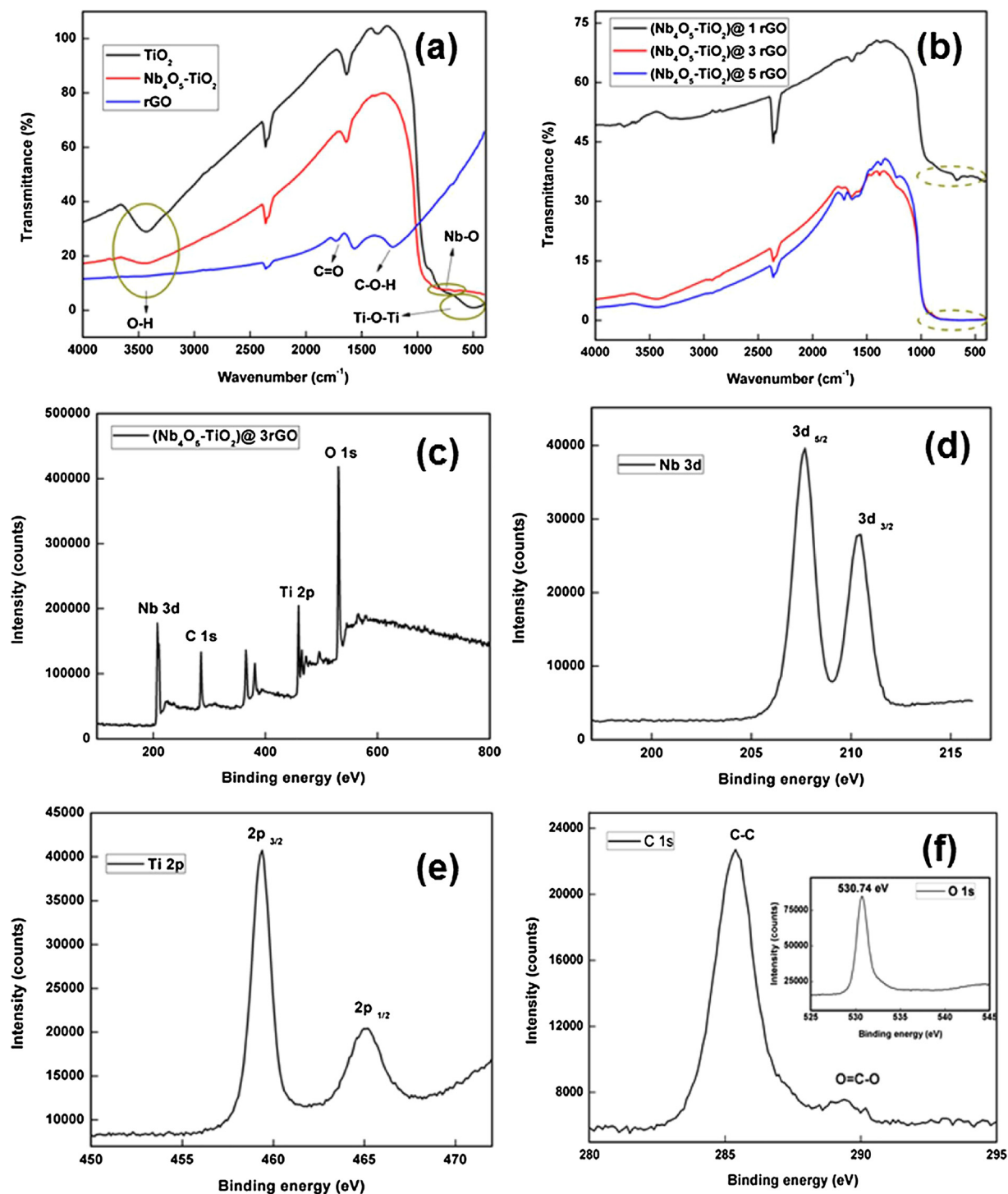


Fig. 5. (a&b) FTIR spectra of TiO_2 , $\text{Nb}_4\text{O}_5\text{-TiO}_2$, rGO and $(\text{Nb}_4\text{O}_5\text{-TiO}_2)\text{@rGO}$ nanocomposites, (c–f) XPS survey spectra of $(\text{Nb}_4\text{O}_5\text{-TiO}_2)\text{@3rGO}$ and high resolution XPS spectra of Nb, Ti, C and O elements.

significantly (3.277–3.221 eV), which strongly influence the photodegradation property of the catalyst. The photodegradation efficiency increased to 75, 75, 83, and 89%, after mixing 1, 2, 3, and 4 wt. % rGO nanosheets with the $\text{Nb}_4\text{O}_5\text{-TiO}_2$ nanorods. Finally, the $(\text{Nb}_4\text{O}_5\text{-TiO}_2)\text{@5rGO}$ photocatalysts exhibited a high photodegradation efficiency of 92% after 180 min UV irradiation. Recently, Safardoust et al. have prepared nitrogen doped graphene quantum dots mixed TiO_2 nanocomposite ($\text{TiO}_2\text{/N-GQDs}$) for photocatalytic application. This group achieved 40% methylene blue degradation when TiO_2 used as the photocatalyst and the degradation efficiency was increased to 85%

while using the $\text{TiO}_2\text{/N-GQDs}$ photocatalyst [47]. Similarly, Sijia and co workers achieved more than 50% MB degradation while using rGO doped TiO_2 photocatalyst under UV light irradiation [48]. Therefore, compared to the metal oxide nanocomposite photocatalyst, the rGO mixed $\text{Nb}_4\text{O}_5\text{-TiO}_2$ nanorods exhibited enhanced photocatalytic performance. An electron rich two dimensional π -conjugated reduced graphene oxide may accept holes and suppress the charge recombination. In addition with this increased surface area ($37.58 \text{ m}^2 \text{ g}^{-1}$) and low energy band gap (3.221 eV) enables $(\text{Nb}_4\text{O}_5\text{-TiO}_2)\text{@5rGO}$ as the good photocatalytic material. This is because of the combination of low

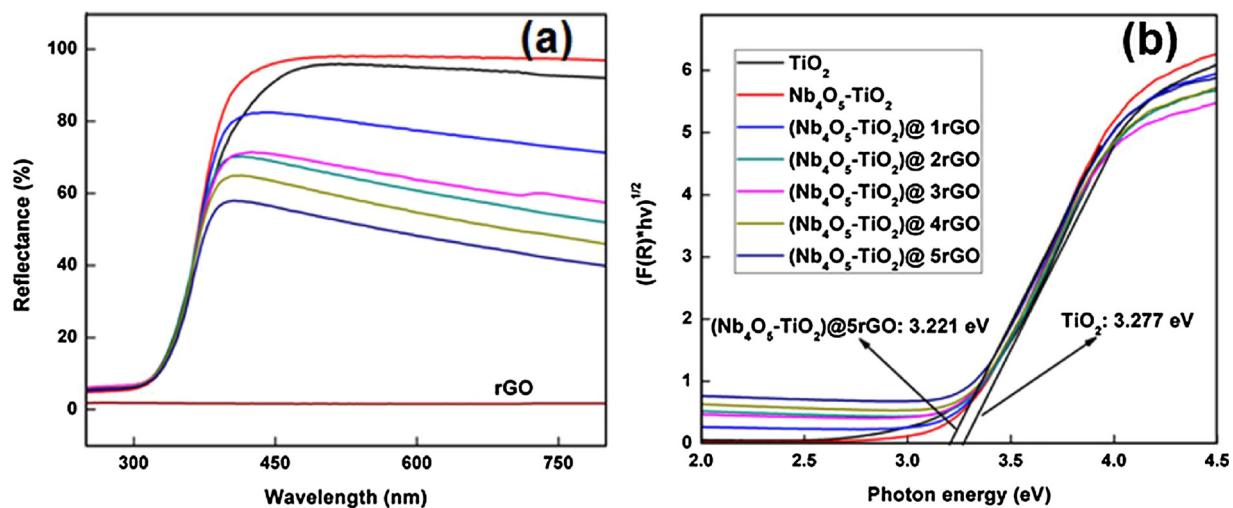


Fig. 6. UV–DRS of (a) reflectance spectra, (b) calculated band gap spectra of TiO_2 , Nb_4O_5 – TiO_2 , rGO and $(\text{Nb}_4\text{O}_5\text{--TiO}_2)$ @rGO nanocomposites.

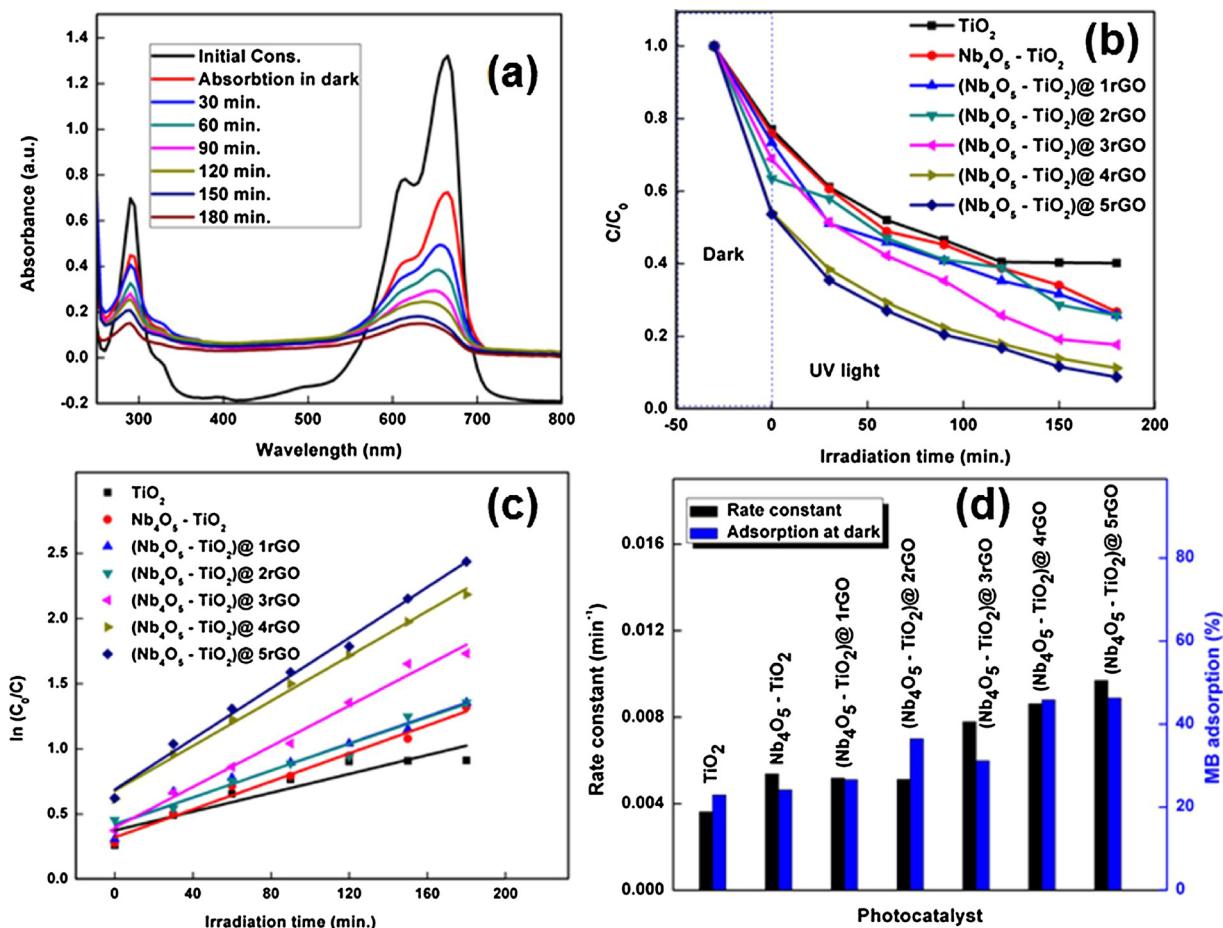


Fig. 7. Absorption spectra of the MB solution in the presence of $(\text{Nb}_4\text{O}_5\text{--TiO}_2)$ @ 5rGO photocatalyst for the different time intervals under UV irradiation (b) change in the concentration of MB as a function of the UV irradiation time with the different samples (c) relationship between $\ln(C_0/C)$ and time (d) apparent first-order rate constant (k) and adsorption capacity of different samples.

band gap (3.221 eV) and high specific surface area. For a better understanding of the photocatalytic efficiency of the photocatalyst, the photocatalytic degradation kinetics of methylene blue was also investigated. The photodegradation reaction rate was approximated by pseudo first-order kinetics and is expressed as [49]

$$\ln(C_0/C) = kt$$

where C_0 and C is the concentration of methylene blue at time $t = 0$ and t , respectively; k is the apparent rate constant (min^{-1}).

Fig. 7c shows the relationship between $\ln(C_0/C)$ and time. The plot of $\ln(C_0/C)$ vs. t was linear for all catalysts, confirming that the photodegradation of MB obeys pseudo first-order kinetics. The apparent rate constant (k) was calculated from the slope of the $\ln(C_0/C)$ vs. time, and Fig. 7d presents the calculated values. The calculated rate constant

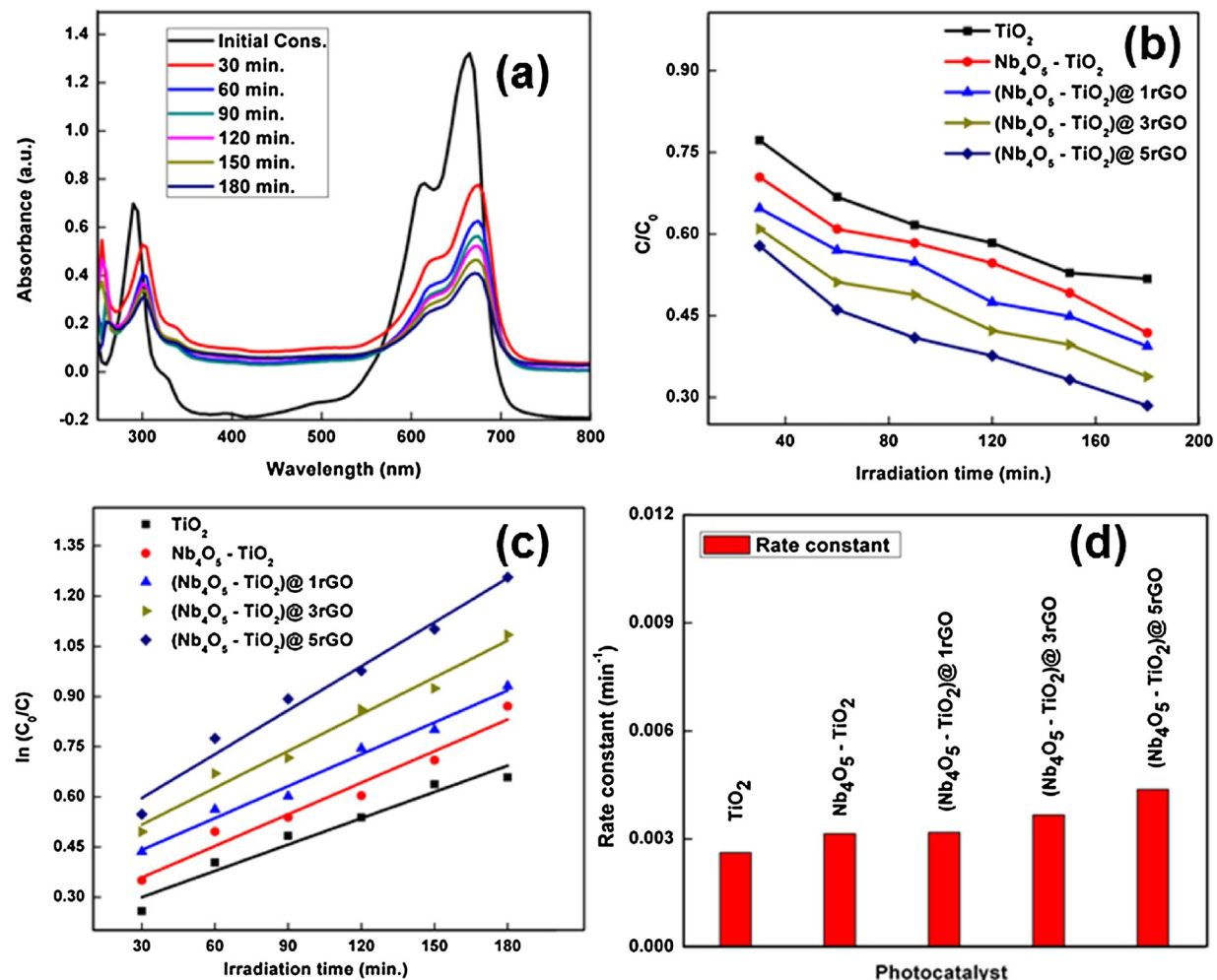


Fig. 8. Absorption spectra of the MB solution in the present of $(\text{Nb}_4\text{O}_5\text{-TiO}_2)@5\text{rGO}$ photocatalyst for the different time intervals under visible light irradiation (b) change in the concentration of MB as a function of the visible light irradiation time with the different samples (c) relationship between the $\ln(C_0/C)$ and time (d) apparent first-order rate constant (k) and adsorption capacity of the different samples.

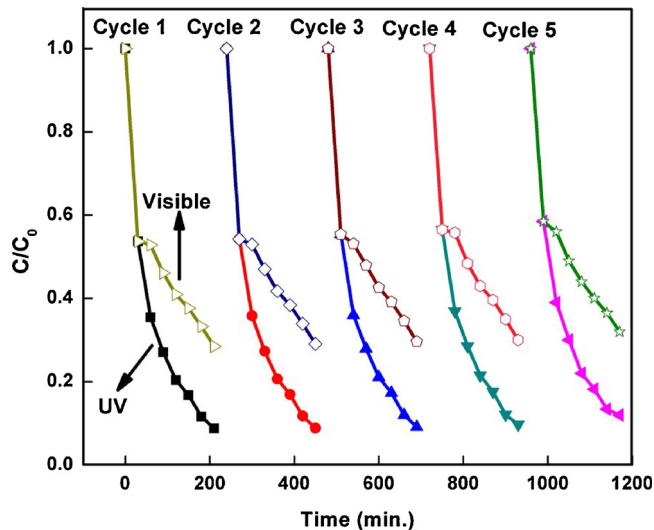


Fig. 9. Recyclability of the photocatalytic decomposition of MB for $(\text{Nb}_4\text{O}_5\text{-TiO}_2)@5\text{rGO}$ photocatalyst under UV and visible light irradiations.

values for TiO_2 , $\text{Nb}_4\text{O}_5\text{-TiO}_2$, $(\text{Nb}_4\text{O}_5\text{-TiO}_2)@1\text{rGO}$, $(\text{Nb}_4\text{O}_5\text{-TiO}_2)@2\text{rGO}$, $(\text{Nb}_4\text{O}_5\text{-TiO}_2)@3\text{rGO}$, $(\text{Nb}_4\text{O}_5\text{-TiO}_2)@4\text{rGO}$ and $(\text{Nb}_4\text{O}_5\text{-TiO}_2)@5\text{rGO}$ nanocomposites are 0.0036, 0.0053, 0.0051, 0.0051, 0.0077,

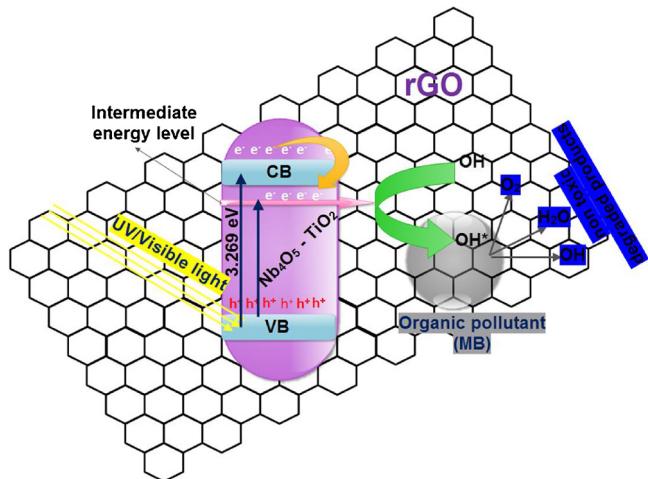
0.0086 and 0.0097 min⁻¹, respectively. The calculations and fitting parameters shows that the reaction rate of the $(\text{Nb}_4\text{O}_5\text{-TiO}_2)@5\text{rGO}$ photocatalyst was faster than the other catalyst materials. The calculated rate constant of $(\text{Nb}_4\text{O}_5\text{-TiO}_2)@5\text{rGO}$ photocatalyst was 0.0097 min⁻¹, which were 2.69 (0.0036 min⁻¹) and 1.83 (0.0053 min⁻¹) times higher than that of pure TiO_2 and $\text{Nb}_4\text{O}_5\text{-TiO}_2$ respectively. The fast reaction rate of the $(\text{Nb}_4\text{O}_5\text{-TiO}_2)@5\text{rGO}$ photocatalyst indicated the excellent removal of methylene blue pollutant. Hence, the introduction rGO nanosheets might extend the light absorption spectrum of $\text{Nb}_4\text{O}_5\text{-TiO}_2$ nanorods by producing an energy level just below the conduction band of $\text{Nb}_4\text{O}_5\text{-TiO}_2$, which is the major rate-limiting factor that controls the photocatalytic efficiency [50]. In addition, the diameter of the photocatalyst (TiO_2 nanorods, $\text{Nb}_4\text{O}_5\text{-TiO}_2$ nanorods and $(\text{Nb}_4\text{O}_5\text{-TiO}_2)@r\text{GO}$) was much smaller than the carrier diffusion length of 60 to 100 nm, which efficiently separates the electron – holes from the catalyst.

Similarly, the photodegradation of methylene blue using TiO_2 , $\text{Nb}_4\text{O}_5\text{-TiO}_2$, $(\text{Nb}_4\text{O}_5\text{-TiO}_2)@1\text{rGO}$, $(\text{Nb}_4\text{O}_5\text{-TiO}_2)@3\text{rGO}$, $(\text{Nb}_4\text{O}_5\text{-TiO}_2)@5\text{rGO}$ photocatalyst under visible light irradiation was studied. Fig. 8a presents the UV absorption spectrum of an aqueous MB solution at various visible light irradiation times with the $(\text{Nb}_4\text{O}_5\text{-TiO}_2)@5\text{rGO}$ photocatalyst. Considerable enhancement of the photocatalytic activity was observed with respect to the addition of rGO nanosheets. The $(\text{Nb}_4\text{O}_5\text{-TiO}_2)@5\text{rGO}$ photocatalyst showed a higher photodegradation efficiency of 72% at the end of 180 min of visible light

Table 2Comparison of the photocatalytic performances of the rGO doped $\text{Nb}_4\text{O}_5\text{-TiO}_2$ composites in this research with that of other TiO_2 composites reported in literatures.

Catalyst material	Light source	Irradiation Time (min.)	Degradation efficiency (%)	Reference
TiO_2	15 W, UV lamp	90	97.6	[51]
Nb_2O_5	500 W Hg lamp	120	89	[52]
$\text{SnO}_2/\text{TiO}_2$	30 W UV lamp	20	95.1	[53]
CNT/TiO_2	100 W Hg lamp	60	> 80	[54]
$\text{Fe}_2\text{O}_3/\text{TiO}_2$	Hg lamp	60	> 95	[55]
$\text{Ag-CNT}/\text{TiO}_2$	20 W UV lamp	60	~75	[56]
Nb_2O_5 doped TiO_2	8W UV lamp	120	76.2	[57]
Nb doped TiO_2	150 W Xe lamp	60	~100	[58]
Nb, N doped TiO_2	150 W Xe lamp	180	~90	[59]
Nb_2O_5 doped TiO_2	400 W, Hg lamp	120	> 95	[60]
$\text{SnO}_2/\text{graphene}$	450 W Xe lamp	360	~100	[61]
GO/BiOBr	300 W Xe lamp	45	~98	[62]
ZnO-rGO	500 W Hg lamp	260	88	[63]
$\text{Cu}_2\text{O}/\text{graphene}$	400 W MH lamp	120	72	[64]
graphene doped TiO_2	450 W Xe lamp	60	> 90	[65]
graphene doped TiO_2	UV lamp	120	> 95	[66]
graphene doped TiO_2	125 W Hg lamp	100	88	[67]
graphene doped TiO_2	Xe lamp	60	82.5	[68]
graphene doped TiO_2	Xe lamp	150	~95	[69]
B,N graphene doped TiO_2	120 W Hg lamp	60	> 90	[70]
$\text{rGO}/\text{TiO}_2/\text{ZnO}$	300 W Xe lamp	120	92	[71]
$\text{Bi-TiO}_2/\text{graphene}$	500 W Halogen lamp	60	95	[72]
$\text{Fe}_3\text{O}_4 @\text{rGO}/\text{TiO}_2$	300W, UV lamp	120	99	[73]
rGO doped $\text{Nb}_4\text{O}_5\text{-TiO}_2$	6 W, UV lamp	180	92	This work

*The degradation efficiency values were obtained/observed from the reported literature.

**Fig. 10.** Schematic diagram of the internal structure and separation of the electron-hole pair in the $(\text{Nb}_4\text{O}_5\text{-TiO}_2)@\text{rGO}$ photocatalyst and MB degradation.

irradiation. Fig. 8b shows the photodegradation efficiency of all photocatalyst materials at various visible light irradiation times. The order of the photodegradation efficiency increased gradually with respect to the addition of rGO nanosheets. Fig. 8c shows a plot of $\ln(C_0/C)$ vs. time. As expected, the plot of $\ln(C_0/C)$ vs. time (t) was linear for all catalysts, which confirmed the photodegradation of MB under visible light irradiation obeys pseudo first-order kinetics. The apparent rate constant (k) of all electrodes was calculated from the slope of the $\ln(C_0/C)$ vs. time plot, and the calculated values are presented in Fig. 8d. The reaction rate of $(\text{Nb}_4\text{O}_5\text{-TiO}_2)@\text{5rGO}$ photocatalyst was faster than that of other catalyst materials and its calculated rate constant value is 0.0043 min^{-1} , which were $1.65 (0.0026 \text{ min}^{-1})$ and $1.38 (0.0031 \text{ min}^{-1})$ times higher than that of the pure TiO_2 and $\text{Nb}_4\text{O}_5\text{-TiO}_2$ nanorods, respectively.

Besides the photocatalytic activity, reusability of the catalyst is also an important factor for practical application. Thus, we investigated the reusability of $(\text{Nb}_4\text{O}_5\text{-TiO}_2)@\text{5rGO}$ catalyst and monitored the

degradation of methylene blue for five consecutive cycles under UV and visible light irradiations. After each MB degradation experiment (180 min.), the photocatalyst was recovered by centrifugation process, and then the separated photocatalyst was washed with double distilled water and acetone. Finally, dried at 80°C for overnight and then used for next cycle. Fig. 9 shows the photodegradation efficiency of $(\text{Nb}_4\text{O}_5\text{-TiO}_2)@\text{5rGO}$ photocatalyst for five successive runs under UV and visible light illuminations. From the reusability experiment we confirmed that $(\text{Nb}_4\text{O}_5\text{-TiO}_2)@\text{5rGO}$ photocatalyst demonstrates its high photocatalytic reusability without an apparent decrease in efficiency. In addition, we compare the photodegradation efficiency of synthesized $(\text{Nb}_4\text{O}_5\text{-TiO}_2)@\text{5rGO}$ with other reported TiO_2 , graphene and niobium composites and as shown in Table 2.

Based on the above research, the photodegradation of MB with the help of the $(\text{Nb}_4\text{O}_5\text{-TiO}_2)@\text{rGO}$ photocatalyst under UV or visible light irradiation may be explained as follows and Fig. 10 shows the corresponding schematic diagram. First, the $(\text{Nb}_4\text{O}_5\text{-TiO}_2)@\text{rGO}$ photocatalyst was excited by the irradiated photon energy that is higher than or equal to the band gap of the $(\text{Nb}_4\text{O}_5\text{-TiO}_2)@\text{rGO}$ nanocomposites. The electrons are excited from the valence band (VB) to the conduction band (CB) followed by the transfer of the photo generated electrons from the CB of $\text{Nb}_4\text{O}_5\text{-TiO}_2$ to the CB of the rGO nanosheets due to the excellent electrical conductivity of the rGO nanosheets. All transferred electrons were stored on rGO and interacted with the surface functional (hydroxyl) groups. After the interaction process, the surface hydroxyl groups (OH) produced hydroxyl radicals (OH^*) on the surface of the $(\text{Nb}_4\text{O}_5\text{-TiO}_2)@\text{rGO}$ photocatalysts. These newly generated hydroxyl radicals (OH^*) act as a strong oxidizing agent and reduce the methylene blue dye [31,74,75]. In addition, the hydroxyl radicals generated further enhance the interactions between the rGO nanosheets and photo generated electrons. This enhances the life time of the charge carriers and the efficiency of $(\text{Nb}_4\text{O}_5\text{-TiO}_2)@\text{rGO}$ photocatalysts. Therefore, the $(\text{Nb}_4\text{O}_5\text{-TiO}_2)@\text{5rGO}$ nanocomposite is a good candidate for photo generated electron – hole pair generation and an efficient pollutant degradation material under UV and visible light irradiation.

3.4. Electrochemical activity

The electrochemical properties of the synthesized TiO_2 ,

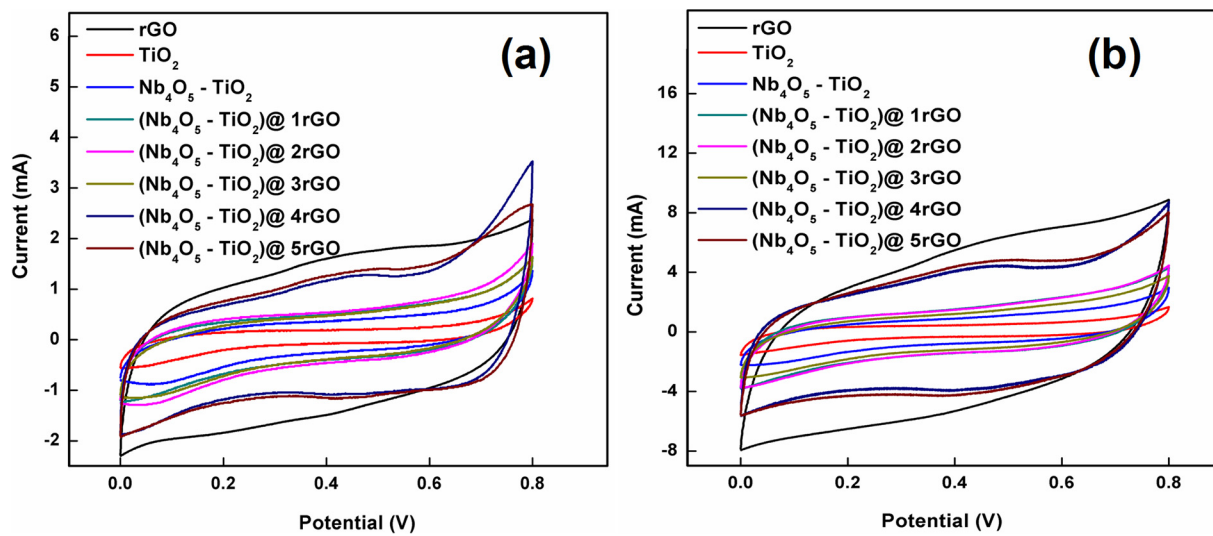


Fig. 11. Cyclic voltammetry plot of all the electrode materials at a scan rate of (a) 20 mV s^{-1} and (b) 100 mV s^{-1} in 1 M Na_2SO_4 aqueous electrolyte.

Table 3

Specific capacitance (C) of all the electrodes in 1 M Na_2SO_4 aqueous electrolyte at different scan rates.

Scan rate (V/s)	Specific capacitance value (C) of all electrodes in 1 M Na_2SO_4 aqueous electrolyte (F g^{-1})													
	TiO ₂	$\text{Nb}_4\text{O}_5\text{-TiO}_2$		$(\text{Nb}_4\text{O}_5\text{-TiO}_2)\text{-1 rGO}$		$(\text{Nb}_4\text{O}_5\text{-TiO}_2)\text{-2 rGO}$		$(\text{Nb}_4\text{O}_5\text{-TiO}_2)\text{-3 rGO}$		$(\text{Nb}_4\text{O}_5\text{-TiO}_2)\text{-4 rGO}$		$(\text{Nb}_4\text{O}_5\text{-TiO}_2)\text{-5 rGO}$		
20	37.19	3.31	77.97	6.94	113.29	10.08	128.75	11.45	106.57	9.48	267.5	23.79	279.38	24.84
40	27.90	2.49	56.49	5.03	88.91	7.91	96.8	8.61	78.52	6.99	223.91	19.91	235.4	20.93
60	24.22	2.16	48.13	4.29	79.07	7.04	83.03	7.39	67.97	6.05	198.03	17.61	145.21	12.91
80	22.23	1.98	43.91	3.91	75.51	6.72	75.4	6.71	62.19	5.53	179.5	15.97	189.18	16.82
100	20.94	1.87	41.97	3.74	73.1	6.51	71.75	6.39	58.79	5.23	167.91	14.94	175.47	15.61

$\text{Nb}_4\text{O}_5\text{-TiO}_2$, and $(\text{Nb}_4\text{O}_5\text{-TiO}_2)\text{-rGO}$ materials were studied by CV, charge-discharge and impedance analysis. Fig. 11a and b present the cyclic voltammograms of all synthesized electrodes recorded at different scan rates under a potential window 0–0.8 V and the CV loop at 20 mV s^{-1} and 100 mV s^{-1} , respectively. The addition rGO to $\text{Nb}_4\text{O}_5\text{-TiO}_2$ provided the rectangular shape and gradually increased the area of the loop. From the CV graph, an ideal rectangular shape with a pair of small redox peaks was observed, confirming the synchronization of EDLC and pseudocapacitive behavior of the electrode materials [76]. The oxidation – reduction peak current also increased gradually with increasing scan rate.

The specific capacitance of the electrode was then calculated using the following equation [31]:

Specific capacitance, $C = (\int idV)/(2m \times \Delta V \times v)$ in F g^{-1} where $\int idV$ is integral areas of the cyclic voltammogram loops; m is the mass of the electrode in g; v is the scan rate in V s^{-1} ; and V is the potential window in volts.

The energy density was calculated using the equation [40],

Energy density, $E = 0.5 C (\Delta V)^2$ in J g^{-1} where C is the specific capacitance in F g^{-1} and ΔV is the potential window size in V.

Table 3 lists the calculated specific capacitance and the energy density value of all the synthesized materials. The specific capacitance of $\text{Nb}_4\text{O}_5\text{-TiO}_2$ (77.97 F g^{-1}) was higher than that of pure TiO_2 nanorods (37.19 F g^{-1}) and increased gradually with increasing addition of rGO, reaching a high specific capacitance of 279.38 F g^{-1} for $(\text{Nb}_4\text{O}_5\text{-TiO}_2)\text{-5rGO}$. The same trend was observed in the energy density values with $(\text{Nb}_4\text{O}_5\text{-TiO}_2)\text{-5rGO}$ showing a high energy density of 28.84 Wh kg^{-1} , which is almost 4 times higher than that of $\text{Nb}_4\text{O}_5\text{-TiO}_2$ (6.94 Wh kg^{-1}). Interestingly, the specific capacitance of $(\text{Nb}_4\text{O}_5\text{-TiO}_2)\text{-4rGO}$ (267.5 F g^{-1}) was closer than that of the $(\text{Nb}_4\text{O}_5\text{-TiO}_2)\text{-5rGO}$ nanocomposite. This was attributed to the re-stacking of rGO nanosheets and separation from the nanorods; this may

decrease the interaction between the nanorods and nanosheets, which diminishes electron transport property slightly. In addition, we have calculated the specific capacitance value rGO nanosheets to understand the increased specific capacitance value of $(\text{Nb}_4\text{O}_5\text{-TiO}_2)\text{-4rGO}$ and $(\text{Nb}_4\text{O}_5\text{-TiO}_2)\text{-5rGO}$ nanocomposite. The calculated specific capacitance value of rGO nanosheet is 331.25 F g^{-1} and 225 F g^{-1} at the scan rate of 20 mV s^{-1} to 100 mV s^{-1} , respectively. The specific capacitance of all the electrodes decreased with increasing scan rates from 20 mV s^{-1} to 100 mV s^{-1} .

The charge-discharge techniques were adopted for all electrodes to examine the electrochemical behavior. Fig. 12a and b show the charge discharge curve of all the electrodes at a current density of 5 A g^{-1} and 25 A g^{-1} .

The specific capacitance and energy density of the electrodes was then calculated using the following equations [77,78]:

Specific capacitance, $C_{sp}^d = I \cdot \Delta t / m \cdot \Delta V$ (from charge-discharge graph)

Energy density, $E = 0.5 C_{sp}^d (\Delta V)^2$ in J/g

Table 4 lists the calculated specific capacitance and energy density of all electrodes. The $(\text{Nb}_4\text{O}_5\text{-TiO}_2)\text{-4rGO}$ and $(\text{Nb}_4\text{O}_5\text{-TiO}_2)\text{-5rGO}$ composite electrodes showed a long discharge time with a symmetric linear slope, indicating better electrochemical character. The pure metal oxide composite (without rGO) electrodes exhibited a shorter discharge time due to the high internal resistivity. After the addition of rGO to the metal oxide composite, the specific capacitance increased gradually with increasing rGO weight percentage. The $(\text{Nb}_4\text{O}_5\text{-TiO}_2)\text{-4rGO}$ and $(\text{Nb}_4\text{O}_5\text{-TiO}_2)\text{-5rGO}$ electrodes exhibiting high specific capacitances of 352.5 F g^{-1} and 365 F g^{-1} , respectively, and their corresponding energy densities were 31.34 Wh kg^{-1} and 32.45 Wh kg^{-1} , respectively. The $(\text{Nb}_4\text{O}_5\text{-TiO}_2)\text{-4rGO}$ and $(\text{Nb}_4\text{O}_5\text{-TiO}_2)\text{-5rGO}$ electrodes shows similar specific capacitances for the reason already discussed in the CV section. Zhang and co workers

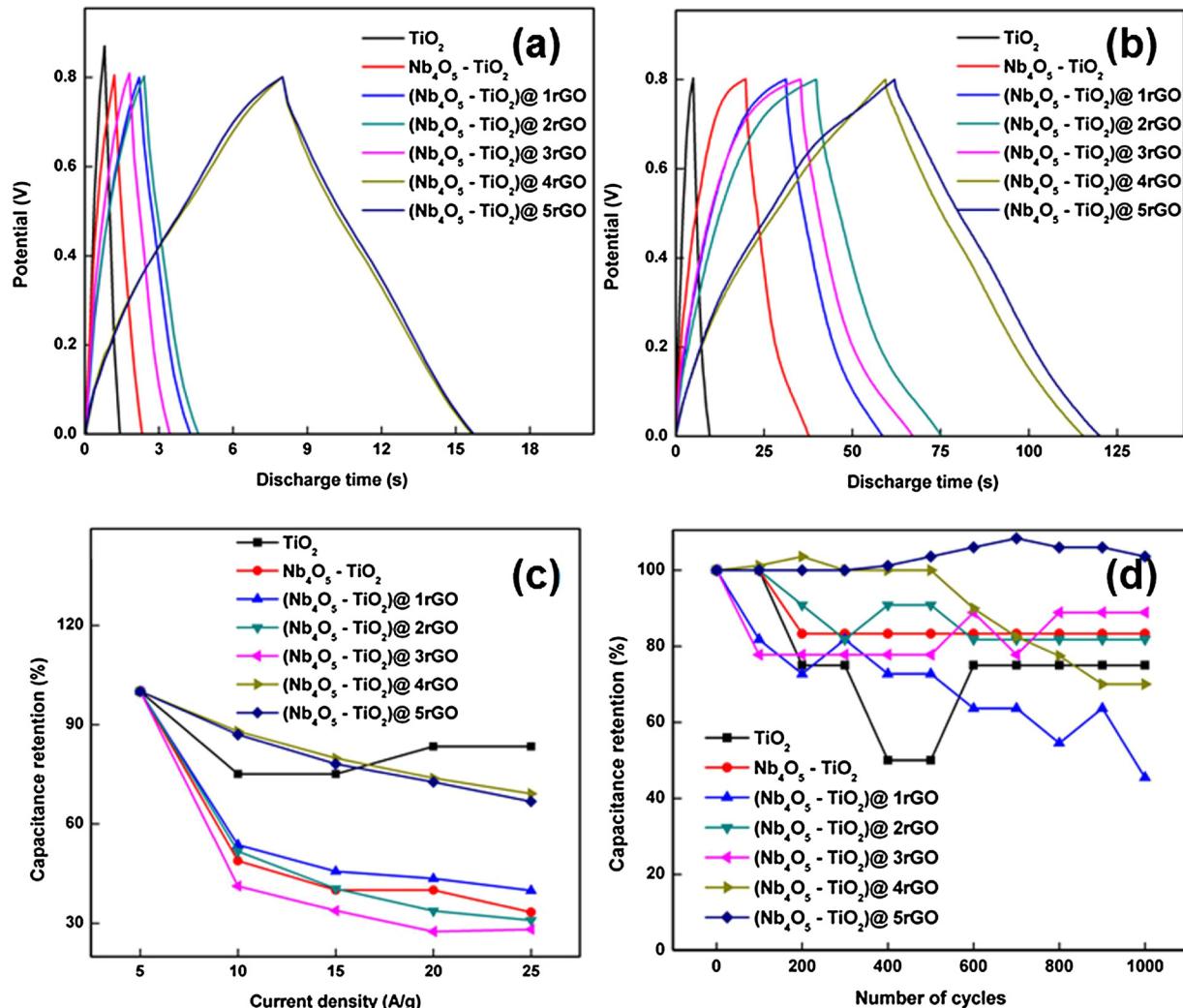


Fig. 12. Charge discharge curves of all the electrodes at a current density of (a) 5 A g^{-1} and (b) 25 A g^{-1} , (c) relationship between the applied current density and specific capacitance retention, (d) cycling stability of all electrode materials at the applied current density of 25 A g^{-1} .

Table 4

Specific capacitance (C_{sp}^d) of all the electrodes in a $1 \text{ M Na}_2\text{SO}_4$ aqueous electrolyte at different applied current densities.

Current density (A/g)	Specific capacitance (C_{sp}^d) of all electrodes in $1 \text{ M Na}_2\text{SO}_4$ aqueous electrolyte (F g^{-1})							
	TiO_2	$\text{Nb}_4\text{O}_5 - \text{TiO}_2$	$(\text{Nb}_4\text{O}_5 - \text{TiO}_2) - 1 \text{ rGO}$	$(\text{Nb}_4\text{O}_5 - \text{TiO}_2) - 2 \text{ rGO}$	$(\text{Nb}_4\text{O}_5 - \text{TiO}_2) - 3 \text{ rGO}$	$(\text{Nb}_4\text{O}_5 - \text{TiO}_2) - 4 \text{ rGO}$	$(\text{Nb}_4\text{O}_5 - \text{TiO}_2) - 5 \text{ rGO}$	
10	30	2.67	112.5	10	172.5	15.34	222.5	19.78
20	22.5	2	55	4.89	92.5	8.23	115	10.23
30	22.5	2	45	4	78.75	7	90	8
40	25	2.23	45	4	75	6.67	75	6.67
50	25	2.23	37.5	3.34	68.75	6.12	68.75	6.12

directly had grown the elongated TiO_2 nanotubes on graphene sheets which show high specific capacitance value of 338 F g^{-1} at a scan rate of 5 mV s^{-1} in $1 \text{ M Na}_2\text{SO}_4$ aqueous electrolyte [79]. Hydrogenated TiO_2 nanoparticles anchored graphene sheets also shown the specific capacitance value of 51.1 F g^{-1} at the current density of 1 A g^{-1} in $1 \text{ M Na}_2\text{SO}_4$ aqueous electrolyte [80]. We observed an enhanced electrochemical performance of $(\text{Nb}_4\text{O}_5 - \text{TiO}_2)@r\text{GO}$ nanocomposite is due to the formation of $\text{Nb}_4\text{O}_5 - \text{TiO}_2$ and rGO interconnected 3D network. In addition, (1) $\text{Nb}_4\text{O}_5 - \text{TiO}_2$ nanorods separates the graphene nanosheets from the agglomeration and (2) well separated rGO nanosheets bind strongly to the $\text{Nb}_4\text{O}_5 - \text{TiO}_2$ nanorods and increase its conductivity by reducing the band gap size; these results in high electrochemical performance [81]. Further, the mesopores between the $\text{Nb}_4\text{O}_5 - \text{TiO}_2$ and

rGO nanosheets may act as an electrolytes reservoir and shorten the electrolyte diffusion. These phenomena gradually increased while increasing the addition of rGO nanosheets to $\text{Nb}_4\text{O}_5 - \text{TiO}_2$. Thus, The $(\text{Nb}_4\text{O}_5 - \text{TiO}_2)@4\text{rGO}$ and $(\text{Nb}_4\text{O}_5 - \text{TiO}_2)@5\text{rGO}$ electrodes showing better electrochemical performance than other lower rGO contented electrodes. These results confirmed that the $(\text{Nb}_4\text{O}_5 - \text{TiO}_2)@r\text{GO}$ nanocomposite exhibits better electrochemical storage capacity than pure TiO_2 and $\text{Nb}_4\text{O}_5 - \text{TiO}_2$ nanorods.

Fig. 12c shows the relationship between the applied current density and the specific capacitance retention of all the electrode materials examined. While increasing the applied current density, the specific capacitance retention decreased gradually because all the active sites are utilized by the electrolyte ions at low applied current densities. The

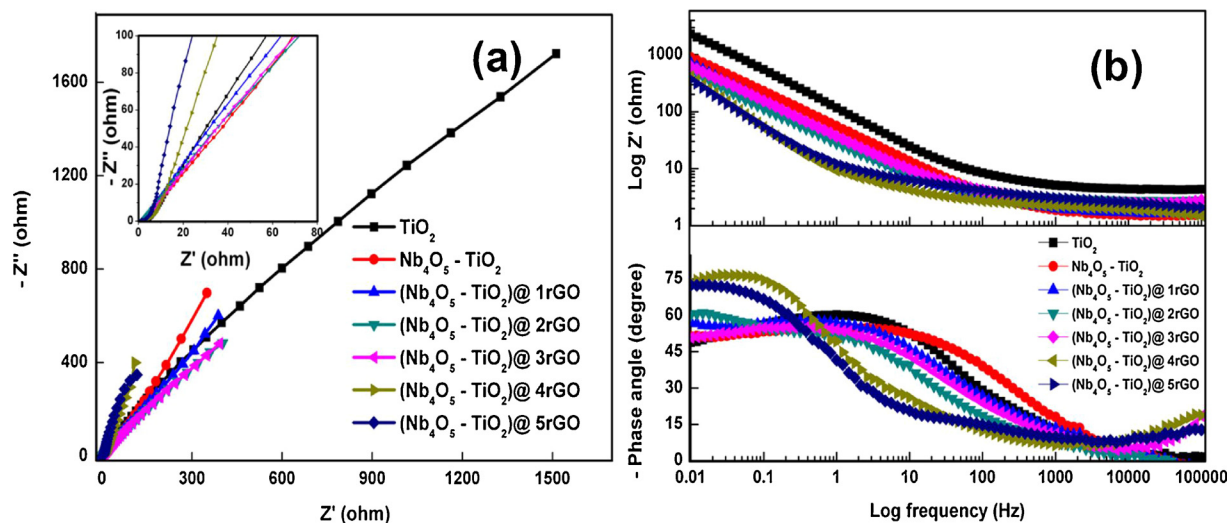


Fig. 13. (a) Nyquist plot and (b) Bode plot of all the electrode materials at 1 M Na_2SO_4 aqueous electrolyte.

Table 5
Impedance parameters calculated from the Nyquist plot.

Scan rate (V/s)	Electrodes						
	TiO_2	$\text{Nb}_4\text{O}_5\text{-TiO}_2$	$(\text{Nb}_4\text{O}_5\text{-TiO}_2)\text{@ 1rGO}$	$(\text{Nb}_4\text{O}_5\text{-TiO}_2)\text{@ 2rGO}$	$(\text{Nb}_4\text{O}_5\text{-TiO}_2)\text{@ 3rGO}$	$(\text{Nb}_4\text{O}_5\text{-TiO}_2)\text{@ 4rGO}$	$(\text{Nb}_4\text{O}_5\text{-TiO}_2)\text{@ 5rGO}$
R_s in Ω	4.32	2.78	1.67	1.56	2.64	2.01	1.40
R_{ct} in Ω	–	–	–	–	–	5.40	4.12
C_{dl} in F/g	0.01	0.02	0.02	0.08	0.91	1.35	2.21
C_F in F/g	46.21	114.02	132.52	164.47	165.19	198.95	228.66

pure TiO_2 nanorods exhibit a better specific capacitance retention value of 83.3% at a current density of 25 A g^{-1} , which is higher than that of any other electrode materials. This is not a surprise because all the active sites are available at the surface of the rod-like structure. Therefore, it is possible to access almost all the active sites by the electrolyte ions even at high applied current densities. Thus, the specific capacitance of the rod-like materials contained electrodes depend on the applied current density. The electrochemical specific capacitance (30 F g^{-1} at the current density of 5 A g^{-1}) of pure TiO_2 nanorods was poor due to its low electrical conductivity. After adding the Nb_4O_5 nanoparticles to the TiO_2 nanorods, the surface become rough (as observed in the FESEM images) by producing pores. These pores helped improve the specific capacitance (112.5 A g^{-1}) of the $\text{Nb}_4\text{O}_5\text{-TiO}_2$ nanorods. Unfortunately, at high scan rates, the electrolyte ions were unable to access the active sites present inside the pores. Hence, the specific capacitance retention of the $\text{Nb}_4\text{O}_5\text{-TiO}_2$ nanorods decreased dramatically to 33.3% at an applied current density of 25 A g^{-1} . The addition of rGO nanosheets to the $\text{Nb}_4\text{O}_5\text{-TiO}_2$ nanorods increase the specific capacitance retention gradually by producing more active sites and providing more electron transfer. Finally, a high 70% capacitance retention was achieved by adding 5 wt. % rGO to the $\text{Nb}_4\text{O}_5\text{-TiO}_2$ nanorods. The cycling stability of the electrode materials was examined at an applied current density of 25 A g^{-1} . Fig. 12d shows the relationship between the specific capacitance retention and the cycle number of all electrode materials. All the electrode materials exhibited a specific capacitance retention of $< 60\%$ after 1000 cycles. In particular, the $(\text{Nb}_4\text{O}_5\text{-TiO}_2)\text{@ 5rGO}$ nanocomposite electrodes exhibited high stability of $\sim 100\%$ after 1000 cycles. The addition of the rGO nanosheets strongly influences the electrochemical stability of the electrode materials. Recently, Zhang et al prepared a 3D TiO_2 – graphene hydro gel through a one pot self-assembly process and achieved more than 100% capacitance retention, even after 2000 cycles [82].

Electrochemical impedance spectroscopy was conducted to study the electrochemical performance of the electrode materials. Fig. 13a

presents the Nyquist plots of all the electrodes. Table 5 lists the series resistance (R_s), charge transfer resistance (R_{ct}), double layer capacitance (C_{dl}), and Faradic capacitance (C_F) of the electrode materials calculated from the Nyquist plot and the corresponding values. Owing to the low primary current distribution, the impedance was calculated at the high frequency region. Similarly, the capacitance was calculated at low frequency region because of its high primary current distribution [31]. All the electrodes exhibited an almost vertical line at the low frequency region, which confirmed the pure capacitive nature. In particular, the addition of rGO to the $\text{Nb}_4\text{O}_5\text{-TiO}_2$ nanorods increases the slope compared to pure or undoped $\text{Nb}_4\text{O}_5\text{-TiO}_2$ nanorods and $(\text{Nb}_4\text{O}_5\text{-TiO}_2)\text{@ 5rGO}$ produced an almost 90° vertical line, indicating ideal EDLC behavior. A small semicircle was also observed at the high frequency region in the $(\text{Nb}_4\text{O}_5\text{-TiO}_2)\text{@ 5rGO}$ and $(\text{Nb}_4\text{O}_5\text{-TiO}_2)\text{@ 5rGO}$ electrodes, confirming the EDLC nature of the rGO nanosheets [83]. The equivalent series resistance of pure TiO_2 is 4.32Ω , which diminishes the electrochemical behavior of the electrode. The R_s value of the $\text{Nb}_4\text{O}_5\text{-TiO}_2$ nanorods and 1, 2, 3, 4, and 5 wt.% of rGO nanosheets added $\text{Nb}_4\text{O}_5\text{-TiO}_2$ nanorods was 2.78, 1.67, 1.56, 2.64, 2.01, and 1.40Ω , respectively. The measured R_{ct} value of the $(\text{Nb}_4\text{O}_5\text{-TiO}_2)\text{@ 4rGO}$ and $(\text{Nb}_4\text{O}_5\text{-TiO}_2)\text{@ 5rGO}$ nanocomposite electrodes were 5.40 and 4.14Ω , respectively. We have calculated the double layer capacitance (C_{dl}) and Faradic capacitance (C_F) of the electrode materials using the imaginary impedance value at high frequency (100 kHz) and low frequency (0.01), respectively [84–87]. Table 5 lists the calculated double layer capacitance (C_{dl}) and Faradic capacitance (C_F) of the electrode materials. All the calculated and measured values followed the specific capacitance trends. Fig. 13b presents the absolute Bode plots ($\log |Z|$ vs. $\log f$) of all the electrodes. From the absolute Bode plot, the slope in the low-frequency region and high-frequency region was 1 and 0, respectively, which confirms the pseudocapacitive and pure resistive behaviors of the electrodes [88]. Similarly, Fig. 13b shows the Bode plot ($\log |Z|$ vs. – phase angle) and the respective graphs of all the electrodes. Here, with the exception of $(\text{Nb}_4\text{O}_5\text{-TiO}_2)\text{@$

4rGO and $(\text{Nb}_4\text{O}_5\text{-TiO}_2)\text{@5rGO}$, the intersect angle at the high and low frequency region was $< 10^\circ$ and $> 45^\circ$, respectively, which represents the resistive and capacitive nature, respectively. Interestingly, the intersect angle of the $(\text{Nb}_4\text{O}_5\text{-TiO}_2)\text{@4rGO}$ and $(\text{Nb}_4\text{O}_5\text{-TiO}_2)\text{@5rGO}$ electrodes were almost 75° , indicating pure capacitive behavior. Therefore, the $(\text{Nb}_4\text{O}_5\text{-TiO}_2)\text{@5rGO}$ composite is a good candidate for fabricating the electrochemical capacitor electrodes [89,90].

4. Conclusion

Novel and structurally stable $(\text{Nb}_4\text{O}_5\text{-TiO}_2)\text{@rGO}$ nanocomposites were synthesized by an ion intercalation-assisted hydrothermal method. Various physio chemical techniques and tools were used to confirm the presence of rGO in the $\text{Nb}_4\text{O}_5\text{-TiO}_2$ nanorods and identify the structural, morphological, surface functional groups, and elemental features of the synthesized $(\text{Nb}_4\text{O}_5\text{-TiO}_2)\text{@rGO}$ nanocomposites. The addition of a high surface area with the good electrical conductivity of the rGO nanosheets improved the characteristics of the $\text{Nb}_4\text{O}_5\text{-TiO}_2$ nanorods. The $(\text{Nb}_4\text{O}_5\text{-TiO}_2)\text{@5rGO}$ nanocomposites delivered an excellent photocatalytic degradation rate towards the degradation of an aqueous MB solution when exposed in UV and visible light irradiation due to the improved photo generated electron-hole pair separation efficiency. In addition, the combination of EDLCs and pseudo capacitance nature of $(\text{Nb}_4\text{O}_5\text{-TiO}_2)\text{@5rGO}$ nanocomposites showed good electrochemical behavior with good cycling stability when used as an electrode for supercapacitors. The strong interaction between the 1D $\text{Nb}_4\text{O}_5\text{-TiO}_2$ nanorods and 2D rGO nanosheets had a synergistic effect in multifunctional applications.

Acknowledgements

This study was supported by the Priority Research Centers Program through the National Research Foundation of Korea (NRF), funded by the Ministry of Education, Science and Technology (MEST) of the Korean government (2009-0093818).

References

- S. Vadivel, Nirmalesh Naveen, V.P. Kamalakannan, Peng Cao, N. Balasubramanian, Facile large scale synthesis of Bi_2S_3 nano rods–graphene composite for photocatalytic photoelectrochemical and supercapacitor application, *Appl. Surf. Sci.* 351 (2015) 635–645.
- Narendran Sekar, Ramaraja P. Ramasamy, Recent advances in photosynthetic energy conversion, *J. Photochem. Photobiol. C: Photochem. Rev.* 22 (2015) 19–33.
- Bocheng Qiu, Mingyang Xing, Jinlong Zhang, Mesoporous TiO_2 nanocrystals grown in situ on graphene aerogels for high photocatalysis and lithium-ion batteries, *J. Am. Chem. Soc.* 136 (16) (2014) 5852–5855.
- Ting Zhu, Wu Hao Bin, Yabo Wang, Xu Rong, Xiong Wen David Lou, Formation of 1D hierarchical structures composed of Ni_3S_2 nanosheets on CNTs backbone for supercapacitors and photocatalytic H_2 production, *Adv. Energy Mater.* 2 (12) (2012) 1497–1502.
- Mehmet A. Oturan, Jean-Jacques Aaron, Advanced oxidation processes in water/wastewater treatment: principles and applications. A review, *Crit. Rev. Env. Sci. Technol.* 44 (23) (2014) 2577–2641.
- Petrick A. Soares, F. Tânia, V. Silva, Diego R. Manenti, M. Selene, U. Souza, A. Rui, R. Boaventura, J. Vitor, P. Vilar, Insights into real cotton-textile dyeing wastewater treatment using solar advanced oxidation processes, *Environ. Sci. Pollut. Res. Int.* 21 (2) (2014) 932.
- Alexandra A.P. Mansur, Herman S. Mansur, Fábio P. Ramanery, Luiz Carlos Oliveira, Patterson P. Souza, “Green” colloidal ZnS quantum dots/chitosan nano-photocatalysts for advanced oxidation processes: study of the photodegradation of organic dye pollutants, *Appl. Catal. B: Environ.* 158 (2014) 269–279.
- R. Saravanan, Elisban Sacari, F. Gracia, Mohammad Mansoob Khan, E. Mosquera, Vinod Kumar Gupta, Conducting PANI stimulated ZnO system for visible light photocatalytic degradation of coloured dyes, *J. Mol. Liq.* 221 (2016) 1029–1033.
- Somayeh Azimi, Alireza Nezamzadeh-Ejhieh, Enhanced activity of clinoptilolite-supported hybridized PbS – CdS semiconductors for the photocatalytic degradation of a mixture of tetracycline and cephalaxin aqueous solution, *J. Mol. Catal. A Chem.* 408 (2015) 152–160.
- Zhen Zhang, Zongyu Huang, Long Ren, Yongzhen Shen, Xiang Qi, Jianxin Zhong, One-pot synthesis of hierarchically nanostructured Ni_3S_2 dendrites as active materials for supercapacitors, *Electrochim. Acta* 149 (2014) 316–323.
- Hui Li, Zhenhua Chen, Chun Kwan Tsang, Zhe Li, Xiao Ran, Chris Lee, Biao Nie, et al., Electrochemical doping of anatase TiO_2 in organic electrolytes for high-performance supercapacitors and photocatalysts, *J. Mater. Chem. A* 2 (1) (2014) 229–236.
- Bo Chen, Junbo Hou, Kathy Lu, Formation mechanism of TiO_2 nanotubes and their applications in photoelectrochemical water splitting and supercapacitors, *Langmuir* 29 (19) (2013) 5911–5919.
- Yunhuai Zhang, Peng Xiao, Xiaoyuan Zhou, Dawei Liu, Betzaida Batalla Garcia, Guozhong Cao, Carbon monoxide annealed TiO_2 nanotube array electrodes for efficient biosensor applications, *J. Mater. Chem.* 19 (7) (2009) 948–953.
- Chengkun Xu, Paul H. Shin, Liangliang Cao, Jiamin Wu, Di Gao, Ordered TiO_2 nanotube arrays on transparent conductive oxide for dye-sensitized solar cells, *Chem. Mater.* 22 (1) (2009) 143–148.
- Muhammad Tahir, Chuanbao Cao, Nasir Mahmood, Faheem K. Butt, Asif Mahmood, Faryal Idrees, Sajad Hussain, M. Tanveer, Zulfiqar Ali, Imran Aslam, Multifunctional $\text{g-C}_3\text{N}_4$ nanofibers: a template-free fabrication and enhanced optical, electrochemical, and photocatalyst properties, *ACS Appl. Mater. Interfaces* 6 (2) (2013) 1258–1265.
- Maryam Salari, Konstantin Konstantinov, Hua Kun Liu, Enhancement of the capacitance in TiO_2 nanotubes through controlled introduction of oxygen vacancies, *J. Mater. Chem.* 21 (13) (2011) 5128–5133.
- Xiaobo Chen, Lei Liu, Y.Yu Peter, Samuel S. Mao, Increasing solar absorption for photocatalysis with black hydrogenated titanium dioxide nanocrystals, *Science* 331 (6018) (2011) 746–750.
- Andreas Mattsson, Michael Leideborg, Karin Larsson, Gunnar Westin, Lars Österlund, Adsorption and solar light decomposition of acetone on anatase TiO_2 and niobium doped TiO_2 thin films, *J. Phys. Chem. B* 110 (3) (2006) 1210–1220.
- Junqing Yan, Guangjun Wu, Naijia Guan, Landong Li, $\text{Nb}_2\text{O}_5\text{/TiO}_2$ heterojunctions: synthesis strategy and photocatalytic activity, *Appl. Catal. B: Environ.* 152 (2014) 280–288.
- Davinder S. Bhachu, Sanjayan Sathasivam, Gopinathan Sankar, David O. Scanlon, Giannantonio Cibin, Claire J. Carmalt, Ivan P. Parkin, et al., Solution processing route to multifunctional titania thin films: highly conductive and photocatalytically active Nb:TiO_2 , *Adv. Funct. Mater.* 24 (32) (2014) 5075–5085.
- Baiju Vidyadharan, Panikar Sathyaseelan Archana, Jamil Ismail, Mashitah M. Yusoff, Rajan Jose, Improved supercapacitive charge storage in electrospun niobium doped titania nanowires, *RSC Adv.* 5 (62) (2015) 50087–50097.
- Dustin Bauer, Alexander J. Roberts, Noriyoshi Matsumi, Jawwad A. Darr, Nano-sized Mo- and Nb-doped TiO_2 as anode materials for high energy and high power hybrid Li-ion capacitors, *Nanotechnology* 28 (19) (2017) 195403.
- Nan Zhang, Min-Quan Yang, Zi-Rong Tang, Yi-Jun Xu, Toward improving the graphene–semiconductor composite photoactivity via the addition of metal ions as generic interfacial mediator, *ACS Nano* 8 (1) (2013) 623–633.
- Min-Quan Yang, Nan Zhang, Yi-Jun Xu, Synthesis of fullerene–, carbon nanotube–, and graphene– TiO_2 nanocomposite photocatalysts for selective oxidation: a comparative study, *ACS Appl. Mater. Interfaces* 5 (3) (2013) 1156–1164.
- Yongye Liang, Hailiang Wang, Hernan Sanchez Casalongue, Zhuo Chen, Hongjie Dai, TiO_2 nanocrystals grown on graphene as advanced photocatalytic hybrid materials, *Nano Res.* 3 (3) (2010) 701–705.
- Sanjaya D. Perera, Ruperto G. Mariano, Khiem Vu, Nijem Nour, Oliver Seitz, Yves Chabal, Kenneth J. Balkus Jr, Hydrothermal synthesis of graphene– TiO_2 nanotube composites with enhanced photocatalytic activity, *ACS Catal.* 2 (6) (2012) 949–956.
- Xuan Pan, Yong Zhao, Shu Liu, Carol L. Korzeniewski, Shu Wang, Zhaoyang Fan, Comparing graphene– TiO_2 nanowire and graphene– TiO_2 nanoparticle composite photocatalysts, *ACS Appl. Mater. Interfaces* 4 (8) (2012) 3944–3950.
- Jacob Tse-Wei Wang, James M. Ball, Eva M. Barea, Antonio Abate, Jack A. Alexander-Webber, Jian Huang, Michael Saliba, et al., Low-temperature processed electron collection layers of graphene/ TiO_2 nanocomposites in thin film perovskite solar cells, *Nano Lett.* 14 (2) (2013) 724–730.
- Shixiong Min, Jianhua Hou, Yonggang Lei, Xiaohua Ma, Gongxuan Lu, Facile one-step hydrothermal synthesis toward strongly coupled TiO_2 /graphene quantum dots photocatalysts for efficient hydrogen evolution, *Appl. Surf. Sci.* 396 (2017) 1375–1382.
- Wan-Kuen Jo, Santosh Kumar, Mark A. Isaacs, Adam F. Lee, S. Karthikeyan, Cobalt promoted $\text{TiO}_2\text{/GO}$ for the photocatalytic degradation of oxytetracycline and Congo Red, *Appl. Catal. B: Environ.* 201 (2017) 159–168.
- Rajesh Rajagopal, Yong Seok Lee, Kwang-Sun Ryu, Synthesis and electrochemical analysis of $\text{Nb}_2\text{O}_5\text{/TiO}_2\text{/H-rGO}$ Sandwich type layered architecture electrode for supercapacitor application, 325 (2017) 611–623.
- S.A. Kuznetsov, Electrochemical synthesis of novel niobium and tantalum compounds in molten salts, *In Molten Salts Chemistry* (2013) 311–329.
- Adriana Zaleska, Doped- TiO_2 : a review, *Recent Patents Eng.* 2 (3) (2008) 157–164.
- Ivan Turkevych, Sofya Kosar, Yuriy Pihosh, Kazuma Mawatari, Takehiko Kitamori, Jinhua Ye, Kiyoshi Shimamura, Synergistic effect between TiO_2 and ubiquitous metal oxides on photocatalytic activity of composite nanostructures, *J. Ceram. Soc. Jpn.* 122 (1426) (2014) 393–397.
- Jinyoung Kim, Jaephil Cho, Rate characteristics of anatase TiO_2 nanotubes and nanorods for lithium battery anode materials at room temperature, *J. Electrochem. Soc.* 154 (6) (2007) A542–A546.
- K. Rajasekar, S. Thennarasu, R. Rajesh, R. Abirami, K. Balkis Ameen, A. Ramasubbu, Preparation of mesoporous $\text{TiO}_2\text{/CNT}$ nanocomposites by synthesis of mesoporous titania via EISA and their photocatalytic degradation under visible light irradiation, *Solid State Sci.* 26 (2013) 45–52.
- Moulik, Samik Roy, Ankita Ghatak, Barnali Ghosh, Study of surface chemistry and microstructure of TiO_2 nanostructures on Pt (111)/Si wafer and FTO glass substrates: a comparative approach, *Surf. Sci.* 651 (2016) 175–181.
- Jianbo Yin, Runtian Chang, Yongjun Shui, Xiaopeng Zhao, Preparation and enhanced electro-responsive characteristic of reduced graphene oxide/polypyrrole composite sheet suspensions, *Soft Matter* 9 (31) (2013) 7468–7478.
- Fuzhi Huang, Dehong Chen, Xiao Li Zhang, Rachel A. Caruso, Yi-Bing Cheng, Dual-function scattering layer of submicrometer-sized mesoporous TiO_2 beads for high-efficiency dye-sensitized solar cells, *Adv. Funct. Mater.* 20 (8) (2010) 1301–1305.

[40] Rajesh Rajagopal, Balkis Ameen Kamaludeen, Rajasekar Krishnan, Synthesis and exploration of graphene bubbles for supercapacitor electrodes, *Electrochim. Acta* 180 (2015) 53–63.

[41] Vernon A. Zeitler, Charles A. Brown, The infrared spectra of some Ti-O-Si, Ti-O-Ti and Si-O-Si compounds, *J. Phys. Chem.* 61 (9) (1957) 1174–1177.

[42] Agnieszka Pawlicka, Mohamed Atik, Michel A. Aegeerter, Synthesis of multicolor Nb_2O_5 coatings for electrochromic devices, *Thin Solid Films* 301 (1) (1997) 236–241.

[43] E. Uyanca, A. Gibaud, P. Daniel, D. Sangaa, G. Sevjdusuren, P. Altantsoo, T. Beuvier, Chih Hae Lee, A.M. Balagurov, Structural and vibrational investigations of Nb-doped TiO_2 thin films, *Mater. Res. Bull.* 60 (2014) 222–231.

[44] Hsiao-Chiang Yao, Ming-Chieh Chiu, Du-Cheng Tsai, Chueh-Jung Huang, Fuhs-Sheng Shieh, Effect of annealing on the Nb-doped TiO_2 films prepared by DC/RF cosputtering, *J. Electrochem. Soc.* 155 (9) (2008) G173–G179.

[45] M. Mohamed Jaffer Sadiq, Sankararao Mutiyala, Jayaraman Mathiyarasu, D.Krishna Bhat, RGO/Zn WO_4 /Fe₃O₄ nanocomposite as an efficient electrocatalyst for oxygen reduction reaction, *J. Electroanal. Chem.* 799 (2017) 102–110.

[46] Ahmed Helal, Farid A. Harraz, Adel A. Ismail, Tarek M. Sami, I.A. Ibrahim, Hydrothermal synthesis of novel heterostructured Fe₃O₄/Bi₂S₃ nanorods with enhanced photocatalytic activity under visible light, *Appl. Catal. B: Environ.* 213 (2017) 18–27.

[47] Hossein Safardoust-Hojaghan, Masoud Salavati-Niasari, Degradation of methylene blue as a pollutant with N-doped graphene quantum dot/titanium dioxide nanocomposite, *J. Clean. Prod.* 148 (2017) 31–36.

[48] Lv Sijia, Junmin Wan, Yuewei Shen, Zhiwen Hu, Preparation of superlong TiO_2 nanotubes and reduced graphene oxide composite photocatalysts with enhanced photocatalytic performance under visible light irradiation, *J. Mater. Sci.: Mater. Electron.* (2017) 1–8.

[49] Shengyan Pu, Rongxin Zhu, Hui Ma, Daili Deng, Xiangjun Pei, Fei Qi, Wei Chu, Facile in-situ design strategy to disperse TiO_2 nanoparticles on graphene for the enhanced photocatalytic degradation of rhodamine 6G, *Appl. Catal. B: Environ.* 218 (2017) 208–219.

[50] Li Zhang, Qinghong Zhang, Hongyong Xie, Jiang Guo, Hailong Lyu, Yaogang Li, Zhiguo Sun, Hongzhi Wang, Zhanhu Guo, Electrospun titania nanofibers segregated by graphene oxide for improved visible light photocatalysis, *Appl. Catal. B: Environ.* 201 (2017) 470–478.

[51] M. Agharei, Dina S. Tayeb, Hussein, Synthesis of TiO_2 nanoparticles and their photocatalytic activity for methylene blue, *Am. J. Nanomat.* 3 (2) (2015) 57–63.

[52] F. Hashemzadeh, R. Rahimi, A. Gaffarinejad, Photocatalytic degradation of methylene blue and rhodamine B dyes by niobium oxide nanoparticles synthesized via hydrothermal method, *Int. J. Appl. Chem. Sci. Res.* 1 (7) (2013) 95–102.

[53] Lin-Rui Hou, Chang-Zhou Yuan, Yang Peng, Synthesis and photocatalytic property of Sn₂O₃/TiO₂ nanotubes composites, *J. Hazard. Mater.* 139 (2) (2007) 310–315.

[54] Guohua Jiang, Xiaoyan Zheng, Yin Wang, Tianwen Li, Xinke Sun, Photo-degradation of methylene blue by multi-walled carbon nanotubes/TiO₂ composites, *Powder Technol.* 207 (1–3) (2011) 465–469.

[55] M.A. Ahmed, Emad E. El-Katori, Zarha H. Gharni, Photocatalytic degradation of methylene blue dye using Fe₂O₃/TiO₂ nanoparticles prepared by sol-gel method, *J. Alloys Compd.* 553 (2013) 19–29.

[56] Feng-Jun Zhang, Ming-liang Chen, Oh Won-Chun, Photoelectrocatalytic properties of Ag-CNT/TiO₂ composite electrodes for methylene blue degradation, *New Carbon Mater.* 25 (5) (2010) 348–356.

[57] Behzad Koosgar Kaleji, Rasoul Sarraf-Mamoory, Akira Fujishima, Influence of Nb dopant on the structural and optical properties of nanocrystalline TiO_2 thin films, *Mater. Chem. Phys.* 132 (1) (2012) 210–215.

[58] Jikai Yang, Xintong Zhang, Changhua Wang, Panpan Sun, Lingling Wang, Bin Xia, Yichun Liu, Solar photocatalytic activities of porous Nb-doped TiO_2 microspheres prepared by ultrasonic spray pyrolysis, *Solid State Sci.* 14 (1) (2012) 139–144.

[59] Tanya M. Breault, Bart M. Bartlett, Composition dependence of TiO_2 (Nb, N)-x compounds on the rate of photocatalytic methylene blue dye degradation, *J. Phys. Chem. C* 117 (17) (2013) 8611–8618.

[60] Sudhir S. Arbijur, Ranjith R. Hawaldar, Uttamrao P. Mulik, Dinesh P. Amalnerkar, Preparation, characterisation and photocatalytic activity of Nb₂O₅/TiO₂ coupled semiconductor oxides, *J. Nanoeng. Nanomanuf.* 3 (1) (2013) 79–83.

[61] Humaira Seema, K. Christian Kemp, Vimlesh Chandra, Kwang S. Kim, Graphene-SnO₂ composites for highly efficient photocatalytic degradation of methylene blue under sunlight, *Nanotechnology* 23 (35) (2012) 355705.

[62] S. Vadivel, M. Vanitha, A. Muthukrishnaraj, N. Balasubramanian, Graphene oxide-BiOBr composite material as highly efficient photocatalyst for degradation of methylene blue and rhodamine-B dyes, *J. Water Process Eng.* 1 (2014) 17–26.

[63] Tian Lv, Likun Pan, Xinxian Liu, Ting Lu, Guang Zhu, Zhuo Sun, Enhanced photocatalytic degradation of methylene blue by ZnO-reduced graphene oxide composite synthesized via microwave-assisted reaction, *J. Alloys Compd.* 509 (41) (2011) 10086–10091.

[64] Weixin Zou, Lei Zhang, Lichen Liu, Xiaobo Wang, Jingfang Sun, Shiguo Wu, Yu Deng, Changjin Tang, Fei Gao, Lin Dong, Engineering the Cu₂O-reduced graphene oxide interface to enhance photocatalytic degradation of organic pollutants under visible light, *Appl. Catal. B: Environ.* 181 (2016) 495–503.

[65] Joon Lee, Seok, Kyeong Hwan You, Chan Beum Park, Highly photoactive, low bandgap TiO_2 nanoparticles wrapped by graphene, *Adv. Mater.* 24 (8) (2012) 1084–1088.

[66] Jiang Du, Xiaoyong Lai, Nailiang Yang, Jin Zhai, David Kisailus, Fabing Su, Dan Wang, Lei Jiang, Hierarchically ordered macro–mesoporous TiO₂–graphene composite films: improved mass transfer, reduced charge recombination, and their enhanced photocatalytic activities, *ACS Nano* 5 (1) (2010) 590–596.

[67] Donglin Zhao, Guodong Sheng, Changjun Chen, Xiangke Wang, Enhanced photocatalytic degradation of methylene blue under visible irradiation on graphene@ TiO_2 dyade structure, *Appl. Catal. B: Environ.* 111 (2012) 303–308.

[68] Wan-Sheng Wang, Dong-Hong Wang, Wen-Gang Qu, Li-Qiang Lu, An-Wu Xu, Large ultrathin anatase TiO_2 nanosheets with exposed {001} facets on graphene for enhanced visible light photocatalytic activity, *J. Phys. Chem. C* 116 (37) (2012) 19893–19901.

[69] Nailiang Yang, Yuanyuan Liu, Hao Wen, Zhiyong Tang, Huijun Zhao, Yuliang Li, Dan Wang, Photocatalytic properties of graphdiyne and graphene modified TiO_2 : from theory to experiment, *ACS Nano* 7 (2) (2013) 1504–1512.

[70] K. Gopalakrishnan, Hrushikesh M. Joshi, Prashant Kumar, L.S. Panchakarla, C.N.R. Rao, Selectivity in the photocatalytic properties of the composites of TiO_2 nanoparticles with B-and N-doped graphenes, *Chem. Phys. Lett.* 511 (4–6) (2011) 304–308.

[71] Nivea Raghavan, Sakthivel Thangavel, Gunasekaran Venugopal, Enhanced photocatalytic degradation of methylene blue by reduced graphene-oxide/titanium dioxide/zinc oxide ternary nanocomposites, *Mater. Sci. Semicond. Process* 30 (2015) 321–329.

[72] Umar Alam, M. Fleisch, Imme Kretschmer, Detlef Bahnemann, M. Muneer, One-step hydrothermal synthesis of Bi-TiO₂ nanotube/graphene composites: an efficient photocatalyst for spectacular degradation of organic pollutants under visible light irradiation, *Appl. Catal. B: Environ.* 218 (2017) 758–769.

[73] Xiaoling Yang, Wei Chen, Jianfei Huang, Ying Zhou, Yihua Zhu, Chunzhong Li, Rapid degradation of methylene blue in a novel heterogeneous Fe₃O₄@rGO@TiO₂ catalyzed photo-Fenton system, *Sci. Rep.* 5 (2015) 10632.

[74] Yuqian Li, Jiangying Qu, Feng Gao, Siyuan Lv, Lin Shi, Chunxiang He, Jingchang Sun, In situ fabrication of Mn₃O₄ decorated graphene oxide as a synergistic catalyst for degradation of methylene blue, *Appl. Catal. B: Environ.* 162 (2015) 268–274.

[75] U.G. Akpan, B.H. Hameed, Parameters affecting the photocatalytic degradation of dyes using TiO₂-based photocatalysts: a review, *J. Hazard. Mater.* 170 (2) (2009) 520–529.

[76] M. Selvakumar, D. Krishna Bhat, Microwave synthesized nanostructured TiO₂-activated carbon composite electrodes for supercapacitor, *Appl. Surf. Sci.* 263 (2012) 236–241.

[77] Sadayappan Nagamuthu, Subbulai Vijayakumar, Gopalan Muralidharan, Synthesis of Mn₃O₄/amorphous carbon nanoparticles as electrode material for high performance supercapacitor applications, *Energy Fuel* 27 (6) (2013) 3508–3515.

[78] Anirban Maitra, Amit Kumar Das, Ranadip Bera, Sumantha Kumar Karan, Sarbaranjan Paria, Suman Kumar Si, Bhanu Bhusan, Khatua, An approach to fabricate PDMS encapsulated all-solid-state advanced asymmetric supercapacitor device with vertically aligned hierarchical Zn–Fe–Co ternary oxide nanowire and nitrogen doped graphene nanosheet for high power device applications, *ACS Appl. Mater. Interfaces* 9 (7) (2017) 5947–5958.

[79] Yimei Zhang, Fei Wang, Hao Zhu, Dandan Zhang, Jie Chen, Elongated TiO_2 nanotubes directly grown on graphene nanosheets as an efficient material for supercapacitors and absorbents, *Compos. Part A: Appl. Sci. Manuf.* 101 (2017) 297–305.

[80] Viet Hung Pham, Thuy-Duong Nguyen-Phan, Xiao Tong, Balasubramanyan Rajagopalan, Jin Suk Chung, James H. Dickerson, Hydrogenated TiO₂@ reduced graphene oxide sandwich-like nanosheets for high voltage supercapacitor applications, *Carbon* 126 (2018) 135–144.

[81] Yangbin Ding, Wei Bai, Jinhua Sun, Yu Wu, Mushtaque A. Memon, Chao Wang, Chengbin Liu, Yong Huang, Jianxin Geng, Cellulose tailored anatase TiO_2 nanospindles in three-dimensional graphene composites for high-performance supercapacitors, *ACS Appl. Mater. Interfaces* 8 (19) (2016) 12165–12175.

[82] Zheye Zhang, Fei Xiao, Yunlong Guo, Shuai Wang, Yunqi Liu, One-pot self-assembled three-dimensional TiO₂-graphene hydrogel with improved adsorption capacities and photocatalytic and electrochemical activities, *ACS Appl. Mater. Interfaces* 5 (6) (2013) 2227–2233.

[83] Hailiang Wang, Joshua Tucker Robinson, Xiaolin Li, Hongjie Dai, Solvothermal reduction of chemically exfoliated graphene sheets, *J. Am. Chem. Soc.* 131 (29) (2009) 9910–9911.

[84] Rajesh Rajagopal, Kwang-Sun Ryu, Facile hydrothermal synthesis of lanthanum oxide/hydroxide nanoparticles anchored reduced graphene oxide for supercapacitor applications, *J. Ind. Eng. Chem.* 60 (2018) 441–450.

[85] F. Lufrano, P. Staiti, Mesoporous carbon materials as electrodes for electrochemical supercapacitors, *Int. J. Electrochem. Sci.* 5 (2010) 903–916.

[86] T. Pajkossy, D.M. Kolb, Double layer capacitance of Pt (111) single crystal electrodes, *Electrochim. Acta* 46 (20–21) (2001) 3063–3071.

[87] Jiahua Zhu, Minjiao Chen, Honglin Qu, Zhiping Luo, Shijie Wu, Henry A. Colorado, Suying Wei, Zhanhu Guo, Magnetic field induced capacitance enhancement in graphene and magnetic graphene nanocomposites, *Energy Environ. Sci.* 6 (1) (2013) 194–204.

[88] Oliver Friedrichs, Juan C. Sánchez-López, Carlos López-Cartes, Thomas Klassen, Ruediger Bormann, Asunción Fernández, Nb₂O₅ “pathway effect” on hydrogen sorption in Mg, *J. Phys. Chem. B* 110 (15) (2006) 7845–7850.

[89] Hee-Chang Youn, Seong-Min Bak, Myeong-Seong Kim, Cherno Jaye, Daniel A. Fischer, Chang-Wook Lee, Xiao-Qing Yang, Kwang Chul Roh, Kwang-Bum Kim, High-surface-area nitrogen-doped reduced graphene oxide for electric double-layer capacitors, *ChemSusChem* 8 (11) (2015) 1875–1884.

[90] Mingia Zhi, Chengcheng Xiang, Jiangtian Li, Ming Li, Nianqiang Wu, Nanostructured carbon–metal oxide composite electrodes for supercapacitors: a review, *Nanoscale* 5 (1) (2013) 72–88.